IEEE Access
Multidisciplinary | Rapid Review | Open Access Journal

Received June 26, 2019, accepted August 6, 2019, date of publication August 12, 2019, date of current version August 23, 2019.

Digital Object Identifier 10.1109/ACCESS.2019.2934638

Enabling Signal Space Diversity for MU-MIMO/OFDMA Cellular Systems That Employ Frequency Diversity

HENRY CARVAJAL MORA[1], (Member, IEEE), NATHALY OROZCO G.[1], (Member, IEEE), PAULO CHILIGUANO T.[2], AND CELSO DE ALMEIDA[3]

[1]Faculty of Engineering and Applied Sciences (FICA), Telecommunications Engineering, Universidad de Las Américas (UDLA), Quito 170125, Ecuador
[2]School of Electronic Engineering and Computer Science (EECS), Queen Mary University of London (QMUL), London E1 4NS, U.K.
[3]School of Electrical and Computer Engineering, University of Campinas (UNICAMP), Campinas 13083-852, Brazil

Corresponding author: Henry Carvajal Mora (henry.carvajal@udla.edu.ec)

This work was supported by the Universidad de Las Américas (UDLA), Quito-Ecuador, as a part of the Research Project ERT.HCM.19.01.

ABSTRACT Signal space diversity (SSD) is a technique to obtain diversity without loss in spectral efficiency. Despite this, SSD has been minimally studied in multiuser scenarios. In this paper, SSD is operated in the uplink of orthogonal frequency division multiple access (OFDMA) cellular systems that exploit frequency diversity, use the optimum maximum-likelihood detector (MLD) and employ antenna arrays at the receivers. Thus, a multiuser multiple-input-multiple-output (MU-MIMO) system that works in presence of own-cell and co-cell interference (CCI) is taken into account. In order to diminish CCI, fractional frequency reuse (FFR) is used in the cellular system. For a feasible MLD implementation, a matrix structure of the received signals is obtained in order to use the sphere decoder algorithm. An exact closed-form expression to calculate the pairwise error probability between two multidimensional symbols is derived. From this, a bit error rate (BER) upper bound is found for single user scenarios. This BER expression is an accurate lower bound for high diversity orders in multiuser scenarios. The BER asymptotic analysis shows that our approach maintains the SSD multidimensional diversity, the spatial diversity of MIMO and the frequency diversity. This allows to overload the system by minimizing the BER and increasing the spectral efficiency, simultaneously.

INDEX TERMS Diversity methods, MIMO, mobile communication, multiple access interference, OFDM.

I. INTRODUCTION

Signal space diversity (SSD) is a technique proposed in [1] to obtain diversity without loss in spectral efficiency. SSD rotates a multidimensional quadrature amplitude modulation (QAM) constellation in such a way that any two constellation points achieve the maximum number of distinct components. When this rotation is carried out properly, the diversity order is equal to the number of dimensions of the constellation. The SSD performance is evaluated in [2] and [3] based on upper bounds to calculate the pairwise-error-probability (PEP). In [4] and [5], bounds to evaluate the SSD symbol error rate (SER) in additive white Gaussian noise (AWGN) and fading channels are obtained. Nevertheless, these bounds become less accurate as the number of dimensions increases.

Due to the improvements that SSD produces in the performance of a system, it has been incorporated in different scenarios. For example, in [6], SSD is proposed to integrate a dual-hop cooperative relay system and to enhance its secrecy performance. In [7], SSD is applied in cognitive networks. Specifically, SSD is used at all transmitting nodes in the secondary network to rotate and interleave the signal components before transmission that enables both source terminals and intermediate relay to transmit different symbols. SSD has been also used in multicarrier systems. In [8], a novel coordinate interleaving scheme between subcarriers is applied to an orthogonal frequency division multiplexing (OFDM) system in order to exploit SSD. For this, binary phase-shift keying (BPSK) modulation is considered. Assuming Rayleigh fading, the authors derive an expression to evaluate the bit

The associate editor coordinating the review of this article and approving it for publication was Wei Xu.

error rate (BER) of the proposed scheme. It is interesting to see that SSD has been recently incorporated even in underwater systems [9]. Hence, rotated constellations are also used in underwater acoustics channels to obtain diversity. In this work, a Max-Log demapper is developed in order to reduce the complexity detection.

In the scenarios described above, there is no presence of interference between users, or multiple access interference (MAI). Generally, SSD has been minimally studied in multiuser scenarios because it is necessary to employ a maximum-likelihood detector (MLD) at the receiver, which is characterized by its exponential complexity [10]. However, in [11], SSD is exploited in a single-carrier and single-cell multiuser scenario by using the sphere decoder (SD) [12] in order to decrease the MLD complexity. SD transforms the decoding process into a tree search algorithm. In addition, in [11], an approximate expression to evaluate the BER for a single user scenario is obtained. Thus, this expression ignores the presence of interference. At this point, it is important to emphasize that cellular systems are not only disrupted by interference from the cell itself (MAI), but also by interference from neighboring cells (co-cell interference, CCI) due to the channel reuse. The latter type of interference is not considered in the work cited previously.

Another technique that uses SSD to mitigate MAI is sparse code multiple access (SCMA), which is a current approach that employ SSD for creating codebooks [13] and it is also a candidate for fifth generation (5G) of cellular systems [14]. With SCMA, different data streams are mapped into codewords of different multidimensional codebooks. Each codeword represents a spread transmission layer. Consequently, data streams share the same time-frequency resources of an orthogonal frequency division multiple access (OFDMA) system. SCMA also employs a suboptimal detector called message passing algorithm (MPA) [15]. Thus, SCMA obtains the diversity from SSD [13]. Nonetheless, in a multicarrier system, it is also possible to obtain frequency diversity transmitting the same symbol on different subcarriers [16]. Hence, a more efficient multicarrier system should be able to guarantee not only the diversity of the rotated constellations but also the frequency diversity.

Some techniques to mitigate CCI have been proposed [17], [18]. The reuse of channels in different cells stands out among these. The approach usually adopted is hard reuse, where the system bandwidth is split into a number of sub-bands according to a chosen reuse factor. Despite hard reuse supports neighboring cells transmit on different sub-bands, it experiences reduced spectral efficiency [19]. As consequence, fractional frequency reuse (FFR) has been proposed as an efficient inter-cell interference coordination (ICIC) technique for Long Term Evolution Advanced (LTE-A) systems [20]. FFR divides the bandwidth into several sub-bands, which are allocated in a smart manner in the cells to reduce the CCI. In general, interference in the uplink is greater than that in the downlink [21], [22]. Hence, the uplink is selected to analyze the performance of FFR schemes.

Another advanced technique for cellular systems is multiple-input-multiple-output (MIMO), which is implemented via antenna arrays. MIMO allows systems to obtain diversity and to increase the spectral efficiency [23] because several users transmit on the same channel. In this case, the technique is known as multiuser MIMO (MU-MIMO). Some works have studied MIMO operating with SSD. In [24], a layered MIMO-OFDM system with SSD is designed. Specifically, a transceiver based on enhanced coordinate interleaving and MLD detection is proposed. The transceiver is evaluated considering only two-dimensional QPSK modulation and the results are validated by employing simulations, which show that the proposal allows to maintain the spatial diversity of MIMO and the space diversity of SSD. In [25], the authors have evaluated the system capacity by considering a symmetric MIMO system that employs SSD and a sub-optimal iterative detector at the receiver. In addition, the system BER is evaluated just by simulations. Moreover, in [26], the performance of SSD for spatial multiplexing is assessed employing a metric named as diversity multiplexing trade-off (DMT) [27], which is the ratio between the diversity order and the multiplexing gain. In [28], [29], SSD is incorporated into a MIMO system employing phase-shift-keying (PSK) modulation and transmit antenna selection (TAS). As TAS is employed, it is not produced interference in the reception, as consequence, maximal ratio combining is employed in the receiver. With this technique and by considering correlated receive antennas, the authors obtain an expression to evaluate the PEP. The results are evaluated for one-dimensional BPSK and two-dimensional QPSK modulations and they show that SSD allows to mitigate the effects of the correlation between the antennas in the receiver. Specifically, a gain is obtained in terms of signal-to-noise ratio (SNR), but the BER curves maintain a diversity similar to the scenario in which SSD is not used. This suggests that, in order to counteract the effects of antenna correlation, SSD sacrifices its diversity. Another recent work related with MIMO and SSD considers zero-forcing precoding with signal space diversity under antenna correlation [30]. Specifically, a $2 \times M$ MIMO system employing a rotated one-dimensional BPSK modulation is considered. The author indicates that a practical example of the considered system model can be a downlink sensor network where a base station communicates with a sensor node. In such a case, the transmit antennas can be arranged with enough spacing such that no spatial correlation exists at the transmit side. On the other hand, the limited sensor size restricts the receiver to position its antennas with sufficient spacing. In this work, the results show that SSD yields a noteworthy improvement on the BER with just a low increase in complexity. Furthermore, in the results, it is interesting to observe that the correlation between the reception antennas produces floors in the BER curves when they are plotted as a function of the SNR. These floors appear in higher BER values when the correlation between

the antennas increases. The works mentioned above consider a single transmitter and a single receiver with several antennas at both sides.

By the above, the main aim of this work is to enable the SSD operation in a multiuser multicarrier cellular system that also exploits frequency diversity and spatial diversity, the latter through MIMO. For this, the first challenge is to establish how the receiver must separate SSD signals transmitted by different users and that are received at different antennas, considering that SSD rotates the constellations and requires interleaving for diversity. Hence, a way to use the SSD approach in the uplink of OFDMA cellular systems employing MLD at the receiver is determined in this work. Thus, the optimum system performance is guaranteed. In addition, it is assumed an OFDMA system that exploits frequency diversity by transmitting the same symbol on several subcarriers. For this, it is considered that some users transmit simultaneously on the same group of subcarriers. Moreover, an antenna array is assumed at the receiver in the base station (BS). Consequently, a MU-MIMO system is studied. Because the system operates in a cellular scenario, there is presence of MAI and CCI. Therefore, another aspect taken into consideration is the way in which this last type of interference is mitigated. For this, FFR is used in the system model.

The matrix structure of all the received signals is developed in order to apply the SD algorithm at the receiver. For this algorithm, an expression to calculate the initial hypersphere radius is also obtained. For the analysis, perfect channel state information (CSI) at the receiver is assumed motivated by the fact that previous works have also considered this scenario and have not been able to find exact expressions to evaluate the SSD performance. Thus, another aim of this work is to find exact expressions to evaluate this kind of technique. In particular, an expression to evaluate the mean signal-to-noise-plus-interference ratio (SNIR) for the proposed system is derived. Then, an exact closed-form expression to evaluate the PEP between two multidimensional symbols in single user scenarios is determined. Specifically, we refer to a single user scenario when a single user within a cell transmits on a group of subcarriers. However, this does not neglect the fact that other users transmit in the co-cells. Therefore, this expression considers the presence of CCI. From the PEP result, a mean BER upper bound is obtained. By simulations, it is shown that under certain considerations, the derived BER expression is an accurate lower bound for multiuser scenarios. The asymptotic performance of the BER is also analyzed in this work in order to obtain the total system diversity. With the results of the asymptotic analysis, it is further evidenced that the optimum rotation angle of the QAM constellations used in SSD can vary depending on the system parameters.

The remainder of this paper is outlined as follows. System and channel models are described in Section II. The matrix structure of received signals is obtained in Section III. In Section IV, the matrix structure is used to implement MLD at the receiver. In Section V, expressions to calculate the PEPs and the BER are derived. The asymptotic analysis of the mean BER is performed in Section VI. Numerical results and discussions are carried out in Section VII. Finally, the main conclusions of the paper are made in Section VIII.

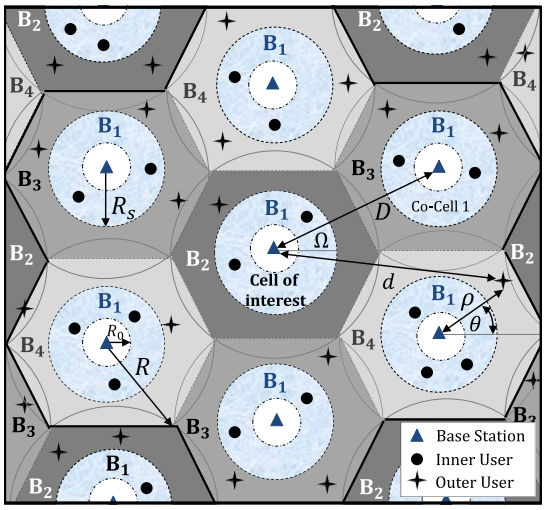

FIGURE 1. Cellular system model.

In what follows, lowercase letters x, bold lowercase letters $\mathbf{x}$ and bold uppercase letters $\mathbf{X}$ denote scalars, vectors and matrices, respectively. In addition, $\mathbf{I}_x$ is a $x \times x$ identity matrix, $\|\cdot\|$ denotes Euclidean norm, $(\cdot)^T$ denotes transpose, $(\cdot)^H$ is conjugate transpose, $\otimes$ represents Kronecker product and $(\cdot)!$ denotes factorial. Moreover, $\Re\{\cdot\}$ and $\Im\{\cdot\}$ represent the real and imaginary parts of their arguments, respectively. Additionally, $\lfloor\cdot\rfloor$ and $\lceil\cdot\rceil$ denote floor and ceil operations, respectively, $\ln(\cdot)$ is natural logarithm and $\overline{X}$ or $\mathrm{E}[X]$ denote the mean value of the random variable X. Finally, $\mathrm{P}(\cdot)$ is the probability operator and $\mathbf{i} = \sqrt{-1}$.

II. SYSTEM AND CHANNEL MODELS

The system and channel models are described in this section.

A. CELLULAR SYSTEM MODEL

Fig. 1 shows the cellular system model, where each circular cell has an inner radius R_0, an outer radius R and a BS at its center. The distance between the center of two co-cells is given by [21]

$$D = R\sqrt{3\mathcal{F}}, \tag{1}$$

where $\mathcal{F}$ is the channel reuse factor. FFR is employed, hence, the cell inner region (CIR) employs reuse factor $\mathcal{F}_\mathrm{i} = 1$ and the cell outer region (COR) uses reuse factor $\mathcal{F}_\mathrm{o} = 3$ [31]. In Fig. 1, R_s is the cell reuse radius and B_k is the k-th frequency sub-band allocated to each cell region. The central cell is the cell of interest receiving interference from co-cells.

Users are uniformly distributed in the cell area. The distance between k-th user and its BS is denoted by ρ_k. As this distance is a random variable, its probability density function (PDF) can be written as

$$f(\rho; R_\mathrm{i}, R_\mathrm{f}) = \frac{2\rho}{R_\mathrm{f}^2 - R_\mathrm{i}^2}, \quad R_\mathrm{i} \le \rho \le R_\mathrm{f}, \tag{2}$$

where R_{i} and R_{f} denote the inner and outer radius for a given cell region, respectively. For better understanding of the following consider Fig. 1. Hence, for the CIR, we have that $R_{\mathrm{i}} = R_0$ and that $R_{\mathrm{f}} = R_s$. On the other hand, for the COR, $R_{\mathrm{i}} = R_s$ and $R_{\mathrm{f}} = R$. Consequently, from (2), the PDF of ρ in the CIR is $f(\rho; R_0, R_s)$ and in the COR is $f(\rho; R_s, R)$. Moreover, the angle formed by the horizontal axis and the k-th user position is denoted by θ_k and its PDF is given by

$$f(\theta) = \frac{1}{2\pi}, \quad 0 \leq \theta < 2\pi. \tag{3}$$

If the location of the ℓ-th interferer in the j-th co-cell is known, the distance between that interferer and the BS in the cell of interest is

$$d_{\ell,j} = \sqrt{D^2 + \rho_{\ell,j}^2 + 2D\rho_{\ell,j}\cos\left[\theta_{\ell,j} - \Omega - (j-1)\frac{\pi}{3}\right]}, \tag{4}$$

where $\Omega = \pi(\mathcal{F}+1)/12$.

B. TRANSMITTER AND RECEIVER MODELS

In the transmitter, a block of m bits is mapped onto a $\mathcal{D}$-dimensional QAM symbol, $\mathbf{s}$, employing Gray encoding in each dimension. A symbol vector is denoted by $\mathbf{s} = (s_1, s_2, \ldots, s_{\mathcal{D}})^T$, where $s_i = \pm 1, \pm 3, \ldots, \pm(\sqrt{M}-1)$, $\forall i$. This symbol vector is transmitted over $\mathcal{D}/2$ time slots (two dimensions in each slot). The time slot duration is T_s. The two-dimensional M-QAM symbols transmitted over each time slot has order $M = 2^{2m/\mathcal{D}}$ and normalized mean power ($\overline{s^2} = 1$). The rotated symbol vector, $\mathbf{r}$, is obtained by $\mathbf{r} = \mathbf{W}^T\mathbf{s}$, where $\mathbf{W}$ is a $\mathcal{D} \times \mathcal{D}$ orthogonal rotation matrix. For $\mathcal{D} \leq 4$, the rotation matrices presented in [1, Section VI] are considered. These matrices have some parameters represented with the variable λ. The values for these parameters must be selected so that a diversity of order $\mathcal{D}$ is obtained. For $\mathcal{D} = 6$, the rotation matrix is[1]

$$\mathbf{W} = \frac{1}{\mathcal{N}}\begin{pmatrix} a & b & c & -x & -y & -z \\ b & c & a & -y & -z & -x \\ -c & -a & -b & z & x & y \\ x & y & z & a & b & c \\ y & z & x & b & c & a \\ -z & -x & -y & -c & -a & -b \end{pmatrix}, \tag{5}$$

where

$$a = \frac{1+\lambda_3}{1+\lambda_3+\lambda_3^2}, \quad b = \lambda_3 a, \; c = \frac{-\lambda_3}{1+\lambda_3}a,$$
$$x = \lambda_6, \quad y = \frac{b-a-\sqrt{(b-a)^2+(a-c)(b-c)}}{a-c}x,$$
$$z = \frac{-xy}{x+y}, \quad \mathcal{N} = \sqrt{a^2+b^2+c^2+x^2+y^2+z^2}.$$

The optimum values of λ_3 and λ_6 for different QAM modulations are detailed in Subsection VII-A.

[1]This rotation matrix is obtained following the guidelines of [1].

In order to obtain SSD, vector $\mathbf{r}$ components must be affected by independent fadings.[2] Thus, a component-wise interleaver is applied at the transmitter.

To obtain frequency diversity, a symbol is transmitted on a group of G subcarriers. For this, the central frequencies of these subcarriers are separated a frequency interval Δ_{fi}, which is greater than the channel coherence bandwidth, B_c. Thus, a frequency domain interleaving is applied. The block diagram of the transmitter in the k-th user equipment (UE) is shown in Fig. 2, where $p(t)$ is a base-band pulse. The figure also shows an example of the interleaving process for $\mathcal{D} = 4$.

It is assumed some users transmitting simultaneously on a same group of subcarriers. In contrast with multicarrier code division multiple access (MC-CDMA) [32], spreading sequences are not used in our approach because signals transmitted in different subcarriers and by different users are affected by independent channel gains, which allow to differentiate them in the detection process. In order to maintain orthogonality between subcarriers, users in the same cell using the same group of subcarriers transmit synchronously. In practical OFDMA systems, this is possible due to timing advance algorithms [33].

Third generation (3G) and fourth generation (4G) cellular systems employ highly efficient power controls [34], [35], which can be considered almost perfect. With this fact, a system performing perfect power control is also assumed. In this scenario, the output power of each UE is

$$P_t = \mathcal{K}^{-1}P_{r,0}\rho^{\beta}, \tag{6}$$

where $P_{r,0}$ is the constant received power at the BS from each UE in the same cell, ρ is the distance between a given UE and its BS, $\mathcal{K}$ is the propagation factor and β is the propagation path-loss exponent. In (6), the product $\mathcal{K}^{-1}\rho^{\beta}$ allows the signals transmitted by all UEs to reach the BS with the same power. As will be described in Subsection II-C, the path-loss increases with a power of the distance.

At the BS, a linear array with Υ equally spaced antennas is considered. Typically, in the BS, the antennas can be separated a distance large enough to ensure that signals arriving at different antennas are affected by independent channel gains. Thus, as the uplink is studied, in the following it is assumed that signals arriving at different antennas are affected by independent channel gains, or equivalently, independent fading.

Due to SSD, MLD is used in the receiver to obtain full diversity [10]. Perfect channel state information (CSI) is considered. The receiver structure for a group of G subcarriers is shown in Fig. 3, where phase canceling and deinterleaving are implemented exclusively for single user scenario. In this case, the figure also shows an example of the received samples considering $\mathcal{D} = 4$. When $\mathcal{U} > 1$ users transmit simultaneously on the same group of subcarriers, signals received at the BS from users at different locations are affected by

[2]In wireless systems, fading refers to a specific kind of attenuation which is highly frequency and time dependent.

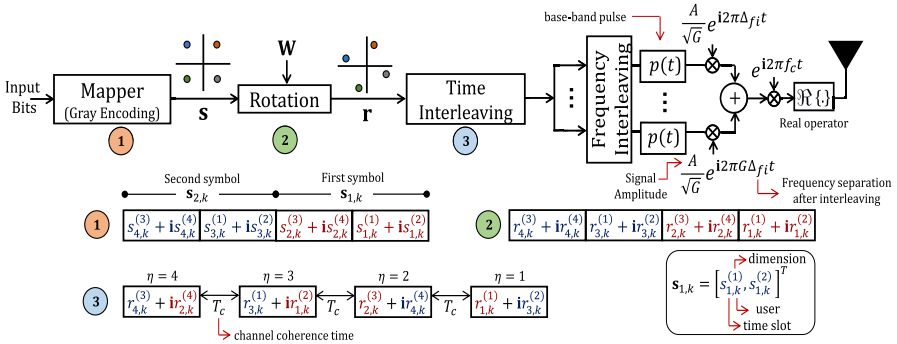

FIGURE 2. Transmitter of the *k*-th UE.

independent channel gains. Because these signals are added by the channel, a phase elimination stage for each user is not viable at the receiver. Phase elimination performed for one user modifies the phases of the received signals of the other users. Hence, deinterleaving cannot be made. Though, it is necessary to detect all received multidimensional symbols regarding that they still remain interleaved. It is important to acknowledge that two different symbols of the same user are interleaved in the transmitter, as shown in Fig. 2.

C. CHANNEL MODEL

A slow frequency-selective Rayleigh fading channel is assumed. The fading is frequency-selective in the total bandwidth, but it is flat in each subcarrier bandwidth. Let $\mathcal{G}_{a,g,\eta,k}$ be the channel gain for a-th antenna, g-th subcarrier, η-th time slot and k-th user. The random variables $\mathcal{G}_{a,g,\eta,k}$ are independent and identically distributed (i.i.d) $\forall\, a$, g, η and k. Channel gains are modeled as zero-mean complex Gaussian random variables with variance $\sigma_{\text{ch}}^2 = 2\sigma^2$, where σ^2 is the variance of the real Gaussian random variables. Hence,

$$\mathcal{G}_{a,g,\eta,k} = \alpha_{a,g,\eta,k} \exp\left(\phi_{a,g,\eta,k}\right), \tag{7}$$

where $\alpha_{a,g,\eta,k}$ is the Rayleigh fading and $\phi_{a,g,\eta,k}$ is the phase uniformly distributed over $[0, 2\pi)$.

Popular models used by wireless carriers for coverage modeling include Okumura-Hata, COST231-Hata [36] and the Stanford University Interim (SUI) path-loss model [37]. All these models imply the power decayment of transmitted signal as a function of the distance between the transmitter and the receiver. Hence, the received power can be written as

$$P_r = \mathcal{K} P_t \rho^{-\beta}, \tag{8}$$

where P_t is the transmitted power and ρ is the distance between the transmitter and the receiver. Further, $\mathcal{K}$ is the propagation factor and β is the propagation path-loss exponent, which depend on the model employed. In the following, the SUI path-loss model is adopted because it operates on the 3.5 GHz band, which is a candidate for 5G networks deployment [38]. With this model, ρ satisfies that 100 m $\leq \rho \leq$ 10000 m and from [37], it is possible to show that

$$\mathcal{K} = \frac{5625}{\pi^2} 2000^{x} f_c^{-(2+x)} 100^{\beta-2} \left(\frac{h_u}{2}\right)^{0.1y}, \tag{9}$$

$$\beta = z_1 - z_2 h_a + \frac{z_3}{h_a}, \tag{10}$$

where f_c is the carrier frequency in MHz, such that $f_c \leq 3500$ MHz, h_a and h_u denote BS antenna height and UE height in meters, respectively, such that 10 m $\leq h_a \leq$ 80 m and 1 m $\leq h_u \leq$ 10 m. Further, $x = 0.6$ when $f_c \geq 2000$ MHz, otherwise, $x = 0$. In addition, y is equal to 0 when $h_u < 2$ m, otherwise, $y = 10.8$ must be employed for intermediate path-loss conditions. For this path-loss conditions, $z_1 = 4$, $z_2 = 0.0065$ and $z_3 = 17.1$ are also used. Other values for these constants are available in [37] for different path-loss environments.

MAI appears because some users transmit on the same subcarriers simultaneously. The number of users transmitting on the same group of G subcarriers in the cell of interest is denoted by $\mathcal{U}$. Moreover, CCI is produced by users in the co-cells transmitting on the same group of subcarriers. The number of interferers in the j-th co-cell, $\mathcal{I}_j$, is a Poisson random variable with mean $\lambda_{\mathcal{I}}$. Lets suppose that CCI comes from the 6 co-cells of the first layer. In scenarios where $\beta \geq 4$, the influence of outer cell layers over CCI becomes negligible [39]. Further, CCI has an asynchronous nature. The instantaneous number of interferers in the co-cells is

$$\mathcal{N}_{\mathcal{I}} = \sum_{j=1}^{6} \mathcal{I}_j. \tag{11}$$

Finally, the received signals are distorted by additive white Gaussian noise (AWGN).

Some assumptions in the channel model allow evaluating the system performance not only by simulations, as in other works in the literature [24], [25], but also the system can be mathematically modeled in order to find expressions to evaluate its performance. From these expressions, some key aspects related with the system behavior can be understood.

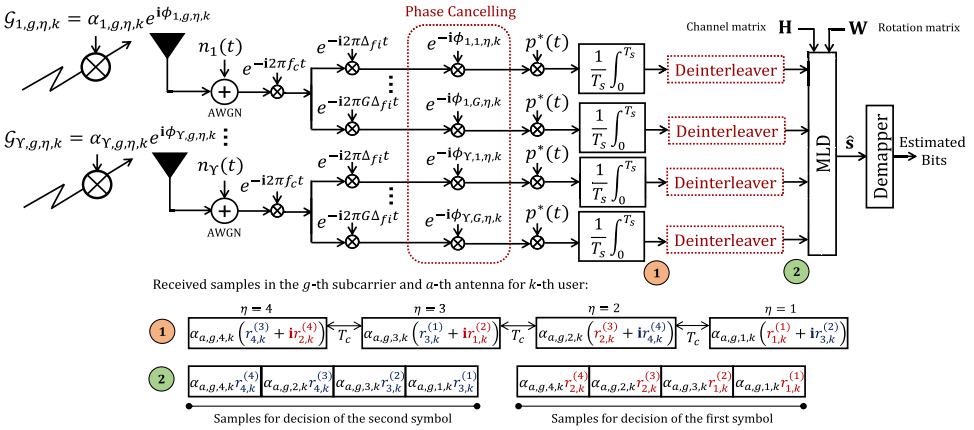

FIGURE 3. Receiver at the BS.

III. MATRIX STRUCTURE OF THE RECEIVED SIGNALS

The matrix structure of the received signals is obtained in this section.

A. SCENARIO $\mathcal{U} = 1$

The total received signals (or samples) at the MLD input can be written as a real $\Upsilon G\mathcal{D}$-dimensional vector, that is[3]

$$\begin{aligned}\mathbf{y} &= \kappa\mathbf{H}\mathbf{r} + \mathbf{C} + \mathbf{n} \\ &= \kappa\mathbf{H}\mathbf{W}^T\mathbf{s} + \mathbf{C} + \mathbf{n},\end{aligned} \tag{12}$$

with

$$\kappa = \frac{A}{2\sqrt{G}}, \tag{13}$$

where A is the signal amplitude, $1/\sqrt{G}$ normalizes the transmitted power per subcarrier, the factor $1/2$ appears due to passband equivalent representation and $\mathbf{n}$ is a $\Upsilon G\mathcal{D}\times 1$ vector with the noise samples, which are modeled as zero mean Gaussian random variables with variance

$$\sigma_n^2 = \frac{N_0}{4T_s}, \tag{14}$$

where N_0 is the unilateral noise power spectral density. The $\Upsilon G\mathcal{D} \times \mathcal{D}$ channel matrix $\mathbf{H}$ is given by

$$\mathbf{H} = \begin{pmatrix} \mathbf{h}_1 & 0 & \dots & 0 \\ 0 & \mathbf{h}_2 & \dots & 0 \\ \vdots & \vdots & \ddots & \vdots \\ 0 & 0 & \dots & \mathbf{h}_{\mathcal{D}} \end{pmatrix}, \tag{15}$$

where

$$\begin{aligned}\mathbf{h}_d = \Big(&\alpha_{1,1,\eta}, \alpha_{1,2,\eta}, \dots, \alpha_{1,G,\eta}, \alpha_{2,1,\eta}, \alpha_{2,2,\eta}, \\ &\dots, \alpha_{2,G,\eta}, \dots, \alpha_{\Upsilon,1,\eta}, \alpha_{\Upsilon,2,\eta}, \dots, \alpha_{\Upsilon,G,\eta}\Big)^T,\end{aligned} \tag{16}$$

[3]Although multidimensional symbols are transmitted in $\mathcal{D}/2$ time slots, we can represent the transmitted symbols as $\mathcal{D}$-dimensional real vectors.

where, for simplicity, the user subscript has been omitted and

$$\eta = \begin{cases} \left\lceil \dfrac{d}{2} \right\rceil, & d \text{ odd} \\ \left\lceil \dfrac{d-1}{2} \right\rceil + \dfrac{\mathcal{D}}{2}, & d \text{ even}, \end{cases} \tag{17}$$

Finally, in (12), $\mathbf{C}$ is a $\Upsilon G\mathcal{D}$-dimensional column vector with the CCI received samples. Considering the examples of transmitted and received samples shown in Fig. 2 and Fig. 3 and by taking into account that signals of co-cell interferers have different phases than the user of interest, the $[(d-1)\Upsilon G + (a-1)G + g]$-th element of $\mathbf{C}$ is given by

$$\begin{aligned}\mathcal{C} = \kappa\,\mathcal{X}\Bigg\{\sum_{\ell=1}^{\mathcal{N}_{\mathcal{I}}}\Big[&\tilde{r}_{d,\ell}\,\mathcal{G}_{a,g,\eta,\ell}\,P(\ell)\exp(-\mathbf{i}\,\phi_{a,g,\eta}) \\ &+ \tilde{r}'_{d,\ell}\,\mathcal{G}'_{a,g,\eta,\ell}\,P'(\ell)\exp(-\mathbf{i}\,\phi'_{a,g,\eta})\Big]\Bigg\},\end{aligned} \tag{18}$$

for $a = 1, 2, \dots, \Upsilon$, $g = 1, 2, \dots, G$ and $d = 1, 2, \dots, \mathcal{D}$, $\mathcal{X}$ represents real operator ($\mathcal{X}\{\cdot\} = \Re\{\cdot\}$) for d odd or imaginary operator ($\mathcal{X}\{\cdot\} = \Im\{\cdot\}$) for d even. Further, η is evaluated by employing (17). In (18), the term into brackets is written as the sum of two terms because CCI is asynchronous. For better understanding refer to Fig. 4. The first term denotes the CCI sample at the time interval $\tau \le t < \zeta_\ell$ and the second term denotes the sample at the interval $\zeta_\ell \le t < \tau + T_s$, where T_s is the time slot duration, τ denotes the delay of the symbol received from the user in the cell of interest and ζ_ℓ is the ℓ-interferer delay that can be modeled as a uniformly distributed random variable over the interval $[\tau, \tau + T_s]$. Moreover, $\tilde{r}_{d,\ell}$ and $\tilde{r}'_{d,\ell}$ denote the complex rotated symbols received from the ℓ-th co-cell interferer, specifically at time intervals $\tau \le t < \zeta_\ell$ and $\zeta_\ell \le t < \tau + T_s$, respectively. Based on the example of Fig. 2 (step ③), the rotated symbol $\tilde{r}_{d,\ell}$ can be

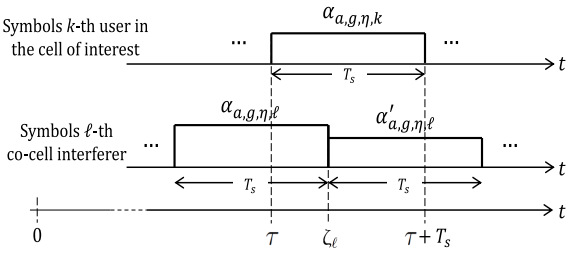

FIGURE 4. Signals arriving at the BS of interest.

written as[4]

$$\tilde{r}_{d,\ell} = \begin{cases} \left[r_{\kappa,\ell}^{(d)} + \mathbf{i}\, r_{\kappa',\ell}^{(d+1)} \right]_{\kappa = \lceil d/2 \rceil,\, \kappa' = \kappa + \mathcal{D}/2}, & d \text{ odd} \\ \left[r_{\kappa,\ell}^{(d-1)} + \mathbf{i}\, r_{\kappa',\ell}^{(d)} \right]_{\kappa' = \lceil (d-1)/2 \rceil,\, \kappa = \kappa' + \mathcal{D}/2}, & d \text{ even.} \end{cases} \tag{19}$$

Finally, in (18), $P(\ell)$ and $P'(\ell)$ are respectively defined as

$$\begin{aligned} P(\ell) &= \sqrt{\rho_\ell^\beta d_\ell^{-\beta}}\, \frac{1}{T_s} \int_\tau^{\zeta_\ell} p(t - \zeta_\ell + T_s) p(t - \tau) dt \\ &= \sqrt{\rho_\ell^\beta d_\ell^{-\beta}} \left(\frac{\zeta_\ell - \tau}{T_s} \right), \end{aligned} \tag{20}$$

$$\begin{aligned} P'(\ell) &= \sqrt{\rho_\ell^\beta d_\ell^{-\beta}}\, \frac{1}{T_s} \int_{\zeta_\ell}^{\tau + T_s} p(t - \zeta_\ell) p(t - \tau) dt \\ &= \sqrt{\rho_\ell^\beta d_\ell^{-\beta}} \left(\frac{\tau + T_s - \zeta_\ell}{T_s} \right), \end{aligned} \tag{21}$$

where it has been considered that $p(t)$ is a unitary amplitude rectangular pulse of duration T_s. In addition, ρ_ℓ^β is the power increase due to power control by considering the link between the ℓ-interferer and the BS in its cell. Moreover, $d_\ell^{-\beta}$ denotes the path-loss attenuation of the link between the ℓ-interferer and the BS in the cell of interest.[5]

B. SCENARIO $\mathcal{U} > 1$

Now, we focus on finding the matrix structure of the received samples for scenarios where $\mathcal{U} > 1$ users are transmitting simultaneously in the same group of G subcarriers. In order to derive the matrix structure of all the received samples, we firstly write the rotation process performed by the k-th UE in matrix form considering that two different multidimensional symbols are interleaved later. Thus, the real $2\mathcal{D}$-dimensional vector containing these two rotated symbols can be written as

$$\mathbf{r}_k = \underbrace{\begin{pmatrix} \mathbf{W}^T & \mathbf{0}_\mathcal{D} \\ \mathbf{0}_\mathcal{D} & \mathbf{W}^T \end{pmatrix}}_{\mathbf{I}_2 \otimes \mathbf{W}^T} \begin{pmatrix} \mathbf{s}_{1,k} \\ \mathbf{s}_{2,k} \end{pmatrix}, \tag{22}$$

where $\mathbf{0}_\mathcal{D}$ is a $\mathcal{D} \times \mathcal{D}$ null matrix and $\mathbf{s}_{\ell,k}$ is the ℓ-th non rotated multidimensional symbol transmitted by k-user before interleaving. Hence, the $\mathcal{D}$ elements of $\mathbf{s}_{\ell,k}$ belong to a $\sqrt{M}$-PAM constellation.

[4]The rotated symbol $\tilde{r}'_{d,\ell}$ can be written in a similar manner.

[5]The factor $\mathcal{K}$ does not appear because power control counterbalances the path-loss multiplying the transmitted power by $\mathcal{K}^{-1}$.

The elements of $\mathbf{r}_k$ can be interleaved employing a $\mathcal{D} \times 2\mathcal{D}$ matrix $\mathbf{E}$. The vector containing the interleaved symbols is obtained as

$$\begin{aligned} \mathbf{r}'_k &= \mathbf{E}\mathbf{r}_k \\ &= \mathbf{E} \left(\mathbf{I}_2 \otimes \mathbf{W}^T \right) \begin{pmatrix} \mathbf{s}_{1,k} \\ \mathbf{s}_{2,k} \end{pmatrix}, \end{aligned} \tag{23}$$

where (22) has been used. For instance, the interleaving matrices for $\mathcal{D} = 2$ and $\mathcal{D} = 4$ can be written respectively as

$$\mathbf{E} = \begin{pmatrix} 1 & 0 & 0 & \mathbf{i} \\ 0 & \mathbf{i} & 1 & 0 \end{pmatrix}, \tag{24}$$

$$\mathbf{E} = \begin{pmatrix} 1 & 0 & 0 & 0 & 0 & \mathbf{i} & 0 & 0 \\ 0 & 0 & 1 & 0 & 0 & 0 & 0 & \mathbf{i} \\ 0 & \mathbf{i} & 0 & 0 & 1 & 0 & 0 & 0 \\ 0 & 0 & 0 & \mathbf{i} & 0 & 0 & 1 & 0 \end{pmatrix}. \tag{25}$$

Matrix $\mathbf{E}$ transforms the real $2\mathcal{D}$-dimensional vector $\mathbf{r}_k$ into the complex $\mathcal{D}$-dimensional vector $\mathbf{r}'_k$. The complex symbols of $\mathbf{r}'_k$ are transmitted in different time slots. Further, notice that the η-th row of $\mathbf{E}$ interleaves the elements of $\mathbf{r}_k$ that are going to be transmitted in the η-th time slot.

By the above, it is possible to show that if $\mathcal{U}$ users are transmitting in the same group of G subcarriers, then the samples received during the η-th time slot can be written as a complex ΥG-dimensional column vector given by

$$\mathbf{y}_\eta = \kappa \mathbf{H}_\eta \mathbf{T}_\eta \mathbf{s}' + \mathbf{C}_\eta + \mathbf{n}_\eta, \quad \eta = 1, 2, \ldots, \mathcal{D}, \tag{26}$$

where $\mathbf{H}_\eta$ is a $\Upsilon G \times \mathcal{U}$ matrix that can be written as

$$\mathbf{H}_\eta = \left(\mathbf{h}_1, \mathbf{h}_2, \ldots, \mathbf{h}_\mathcal{U} \right), \tag{27}$$

with

$$\begin{aligned} \mathbf{h}_k = \big(&\mathcal{G}_{1,1,\eta,k}, \mathcal{G}_{1,2,\eta,k}, \ldots, \mathcal{G}_{1,G,\eta,k}, \mathcal{G}_{2,1,\eta,k}, \mathcal{G}_{2,2,\eta,k}, \\ &\ldots, \mathcal{G}_{2,G,\eta,k}, \ldots, \mathcal{G}_{\Upsilon,1,\eta,k}, \mathcal{G}_{\Upsilon,2,\eta,k}, \ldots, \mathcal{G}_{\Upsilon,G,\eta,k} \big)^T. \end{aligned} \tag{28}$$

Furthermore, $\mathbf{T}_\eta$ is a $\mathcal{U} \times 2\mathcal{D}\mathcal{U}$ matrix written as

$$\mathbf{T}_\eta = \mathbf{I}_\mathcal{U} \otimes \left[\mathbf{E}_\eta \left(\mathbf{I}_2 \otimes \mathbf{W}^T \right) \right], \tag{29}$$

where $\mathbf{E}_\eta$ denotes the η-th row of matrix $\mathbf{E}$. Additionally, in (26), $\mathbf{s}'$ is a $2\mathcal{D}\mathcal{U}$-dimensional column vector given by

$$\mathbf{s}' = \left(\mathbf{s}_{1,1}, \mathbf{s}_{2,1}, \mathbf{s}_{1,2}, \mathbf{s}_{2,2}, \ldots, \mathbf{s}_{1,\mathcal{U}}, \mathbf{s}_{2,\mathcal{U}} \right)^T. \tag{30}$$

Finally, $\mathbf{C}_\eta$ and $\mathbf{n}_\eta$ are complex ΥG-dimensional column vectors with the CCI and noise samples, respectively. The $[(a-1)G + g]$-th element of $\mathbf{C}_\eta$ is

$$\mathcal{C} = \kappa \sum_{\ell=1}^{\mathcal{N}_\mathcal{I}} \left[\tilde{r}_{\eta,\ell}\, \mathcal{G}_{a,g,\eta,\ell}\, P(\ell) + \tilde{r}'_{\eta,\ell}\, \mathcal{G}'_{a,g,\eta,\ell}\, P'(\ell) \right], \tag{31}$$

for $a = 1, 2, \ldots, \Upsilon$ and $g = 1, 2, \ldots, G$. $\mathcal{C}$ is written as a sum of two terms due to CCI asynchronism. In (31), $\tilde{r}_{\eta,\ell}$

and $\tilde{r}'_{\eta,\ell}$ are the complex symbols received from the ℓ-th co-cell interferer during the η-th time slot after rotation and interleaving processes. They arrive at the BS of interest at time intervals $\tau \leq t < \zeta_\ell$ and $\zeta_\ell \leq t < \tau + T_s$, respectively. The rotated and interleaved symbol $\tilde{r}_{\eta,\ell}$ is given by

$$\tilde{r}_{\eta,\ell} = \begin{cases} r_{\eta,\ell}^{(2\eta-1)} + \mathbf{i}\, r_{\eta+\mathcal{D}/2,\ell}^{(2\eta)}, & \eta \leq \mathcal{D}/2 \\ r_{\eta,\ell}^{(2\eta-\mathcal{D}-1)} + \mathbf{i}\, r_{\eta-\mathcal{D}/2,\ell}^{(2\eta-\mathcal{D})}, & \eta > \mathcal{D}/2. \end{cases} \tag{32}$$

The symbol $\tilde{r}'_{\eta,\ell}$ can be written similarly. For better understanding of (32), refer to the interleaver output denoted as ③ in Fig. 2. Finally, in (31), the channel gains $\mathcal{G}_{a,g,\eta,\ell}$ and $\mathcal{G}'_{a,g,\eta,\ell}$ are related to co-cell interferers and they are also associated with time intervals $\tau \leq t < \zeta_\ell$ and $\zeta_\ell \leq t < \tau + T_s$, respectively. Appendix A shows that the variance of the quadrature components of the elements of $\mathbf{C}_\eta$ (CCI variance per channel) is given by

$$\sigma_c^2 = \frac{A^2}{12G} \lambda_{\mathcal{I}}\, \sigma_{\text{ch}}^2\, \overline{s^2}\, \Lambda, \tag{33}$$

where

$$\Lambda = \sum_{j=1}^{6} \mathrm{E}\left[\rho^\beta d^{-\beta}\left(R_\text{i}, R_\text{f}, \mathcal{F}\right)\right]_j, \tag{34}$$

with

$$\begin{aligned} &\mathrm{E}\left[r^\beta d^{-\beta}\left(R_\text{i}, R_\text{f}, \mathcal{F}\right)\right]_j \\ &\quad = \frac{2}{R_\text{f}^2 - R_\text{i}^2} \int_{R_\text{i}}^{R_\text{f}} \rho^{\beta+1} \left(D^2 + \rho^2\right)^{-\frac{\beta}{2}} \\ &\qquad \times {}_2\mathrm{F}_1\left[\frac{\beta}{4}, \frac{\beta+2}{4}; 1; \left(\frac{2D\rho}{D^2+\rho^2}\right)^2\right] d\rho, \end{aligned} \tag{35}$$

where D is given by (1) and ${}_2\mathrm{F}_1(.,.;.;.)$ is the ordinary hypergeometric function [40, Eqs. (9.14.2), (9.100)]. Equation (35) has closed form for even values of β:

$$\mathrm{E}\left[r^\beta d^{-\beta}\left(R_\text{i}, R_\text{f}, \mathcal{F}\right)\right]_j = \frac{\vartheta\left(1-a^2\right) - \vartheta\left(1-b^2\right)}{b^2 - a^2}, \tag{36}$$

where $a = R_\text{i}/D$, $b = R_\text{f}/D$ and

$$\vartheta(x) = \begin{cases} 1 - x + \ln(x), & \beta = 2 \\ 1 - x + \dfrac{5}{x} - \dfrac{1}{x^2} + 4\ln(x), & \beta = 4 \\ 1 - x + \dfrac{27}{x} - \dfrac{37}{2x^2} + \dfrac{8}{x^3} - \dfrac{3}{2x^4} + 9\ln(x), & \beta = 6. \end{cases} \tag{37}$$

The deinterleaving and phase canceling processes performed in the receiver for the scenario $\mathcal{U} = 1$ do not modify the statistics of the received symbols. Hence, the variance of the random variable defined by (18) is also equal to (33).

From (26), the vector containing all the samples received in $\mathcal{D}$ time slots is given by

$$\underbrace{\begin{pmatrix} \mathbf{y}_1 \\ \mathbf{y}_2 \\ \vdots \\ \mathbf{y}_\mathcal{D} \end{pmatrix}}_{\mathbf{y}} = \kappa \underbrace{\begin{pmatrix} \mathbf{H}_1 & \mathbf{0} & \dots & \mathbf{0} \\ \mathbf{0} & \mathbf{H}_2 & \dots & \mathbf{0} \\ \vdots & \vdots & \ddots & \vdots \\ \mathbf{0} & \mathbf{0} & \dots & \mathbf{H}_\mathcal{D} \end{pmatrix}}_{\mathbf{H}} \underbrace{\begin{pmatrix} \mathbf{T}_1 \\ \mathbf{T}_2 \\ \vdots \\ \mathbf{T}_\mathcal{D} \end{pmatrix}}_{\mathbf{T}} \mathbf{s}' + \underbrace{\begin{pmatrix} \mathbf{C}_1 \\ \mathbf{C}_2 \\ \vdots \\ \mathbf{C}_\mathcal{D} \end{pmatrix}}_{\mathbf{C}} + \underbrace{\begin{pmatrix} \mathbf{n}_1 \\ \mathbf{n}_2 \\ \vdots \\ \mathbf{n}_\mathcal{D} \end{pmatrix}}_{\mathbf{n}}, \tag{38}$$

where the $\mathbf{0}$s in the diagonal matrix $\mathbf{H}$ denote $\Upsilon G \times \mathcal{U}$ null matrices, $\mathbf{y}$ is a $\Upsilon G\mathcal{D}$-dimensional column vector, $\mathbf{H}$ is a $\Upsilon G\mathcal{D} \times \mathcal{D}\mathcal{U}$ matrix, $\mathbf{T}$ is a $\mathcal{D}\mathcal{U} \times 2\mathcal{D}\mathcal{U}$ matrix, $\mathbf{s}'$ is given by (30) and finally, $\mathbf{C}$ and $\mathbf{n}$ are $\Upsilon G\mathcal{D}$-dimensional column vectors. Matrix $\mathbf{H}$ contains the fading channel effects and matrix $\mathbf{T}$ contains the rotation and interleaving processes effects for the multiuser scenario.

IV. RECEIVER IMPLEMENTATION

In this section, the matrix structure developed in Section III is employed to implement the MLD at the receiver in the BS.

A. SCENARIO $\mathcal{U} = 1$

Consider the matrix structure given by (12). For high number of co-cell interferers, each element of $\mathbf{C}$ can be modeled by a zero-mean real Gaussian random variable with variance σ_c^2, which is given by (33). Moreover, each element of $\mathbf{n}$ is also a zero-mean real Gaussian random variable with variance σ_n^2, which is given by (14). Under these considerations, the MLD decides by a $\mathcal{D}$-dimensional symbol vector $\tilde{\mathbf{s}}$ by considering the next minimum-distance criterion:

$$\tilde{\mathbf{s}} = \arg\min_{\hat{\mathbf{s}}} \left\| \mathbf{y} - \kappa \mathbf{H}' \hat{\mathbf{s}} \right\|^2, \tag{39}$$

where $\hat{\mathbf{s}}$ is a candidate symbol vector and the $\Upsilon G\mathcal{D} \times \mathcal{D}$ matrix $\mathbf{H}'$ is given by

$$\mathbf{H}' = \mathbf{H}\mathbf{W}^T. \tag{40}$$

For analytical purposes, $\mathbf{H}'$ is an equivalent channel matrix including the effects of the fading channel and the effects of the constellation rotation on the transmitted symbols. It can be shown that (39) requires the evaluation of $\sqrt{M}^\mathcal{D}\left[\Upsilon G\mathcal{D}(\mathcal{D}+1) - 1\right]$ real additions/subtractions and $\sqrt{M}^\mathcal{D} \Upsilon G\mathcal{D}(\mathcal{D}+2)$ real multiplication/divisions.

B. SCENARIO $\mathcal{U} > 1$

Consider the matrix structure of the received samples given by (38). For a high number of co-cell interferers, each element of $\mathbf{C}$ can be modeled by a zero-mean complex Gaussian random variable, whose components have the variance given by (33). Moreover, each element of $\mathbf{n}$ is also a zero-mean

complex Gaussian random variable and their components have the variance given by (14). Therefore, MLD is a multiuser detector deciding by a $2\mathcal{DU}$-dimensional symbol vector $\tilde{\mathbf{s}}$ by employing the minimum-distance criterion:

$$\tilde{\mathbf{s}} = \arg\min_{\hat{\mathbf{s}}'} \left\| \mathbf{y} - \kappa \mathbf{H}' \hat{\mathbf{s}}' \right\|^2, \tag{41}$$

where $\hat{\mathbf{s}}'$ is a candidate symbol vector of the form of (30) and from (38), the $\Upsilon G\mathcal{D} \times 2\mathcal{DU}$ matrix $\mathbf{H}'$ can be written as

$$\mathbf{H}' = \mathbf{HT}, \tag{42}$$

and it contains the fading channel, the interleaving and the constellation rotation for the multiuser scenario. From (41), MLD decides by $2\mathcal{DU}$-multidimensional symbols, that is, $2\mathcal{D}$-multidimensional symbols for each user. The criterion of (41) requires the evaluation of $M^{\mathcal{DU}}\left[\Upsilon G\mathcal{D}(2\mathcal{DU}+1)-1\right]$ complex additions/subtractions and $M^{\mathcal{DU}} 2\Upsilon G\mathcal{D}(\mathcal{DU}+1)$ complex multiplications/divisions.

From the above, MLD can become infeasible for high values of $\mathcal{D}$ or $\mathcal{U}$. On the other hand, SD detector presents the same performance, but with less complexity of the MLD detector. SD transforms the detection into a tree search algorithm [12], which searches for a possible vector $\hat{\mathbf{s}}$ within a hypersphere of radius $\wp$ centered at the received vector $\mathbf{y}$. Hence, it avoids the complexity of the exhaustive search.

SD requires **QR** factorization of matrix $\mathbf{H}'$ of (12) or (38), as appropriate. In the multiuser scenario, if $\mathcal{U} > \Upsilon G/2$, then $\mathbf{H}'$ is rank-deficient. Hence, Tikhonov regularization [41, Eq. (3)] can be used in (41). In this case, SD algorithm uses an extended matrix $\underline{\mathbf{H}}$, which is factorized as

$$\underline{\mathbf{H}} = \begin{pmatrix} \mathbf{H}' \\ \sqrt{\sigma_c^2+\sigma_n^2}\,\mathbf{I}_{2\mathcal{DU}} \end{pmatrix} = \underline{\mathbf{Q}}\,\underline{\mathbf{R}} = \begin{pmatrix} \underline{\mathbf{Q}}_1 \\ \underline{\mathbf{Q}}_2 \end{pmatrix} \underline{\mathbf{R}}, \tag{43}$$

where the $(\Upsilon G\mathcal{D}+2\mathcal{DU})\times 2\mathcal{DU}$ orthonormal columns matrix $\underline{\mathbf{Q}}$ is partitioned into $\underline{\mathbf{Q}}_1$ and $\underline{\mathbf{Q}}_2$ of dimensions $\Upsilon G\mathcal{D} \times 2\mathcal{DU}$ and $2\mathcal{DU} \times 2\mathcal{DU}$, respectively, and $\underline{\mathbf{R}}$ is a $2\mathcal{DU} \times 2\mathcal{DU}$ upper triangular matrix. A technique to perform the above factorization is proposed in [42], which makes an ordering in the $\mathbf{H}'$ columns to further reduce SD complexity. However, it introduces a bias in the SD metrics, but its effects over the system performance are imperceptible [43].

Naming $\mathbf{z} = \underline{\mathbf{Q}}_1^H \mathbf{y}$, a candidate symbol vector is inside of the hypersphere, if it satisfies the condition [12]

$$\begin{aligned} \left\| \mathbf{z} - \kappa \underline{\mathbf{R}} \hat{\mathbf{s}}' \right\|^2 &\le \wp^2 \\ \sum_{\kappa=1}^{2\mathcal{DU}} \left(z_\kappa - \kappa \sum_{\ell=\kappa}^{2\mathcal{DU}} r_{\kappa,\ell} \hat{s}_\ell \right)^2 &\le \wp^2, \end{aligned} \tag{44}$$

where $r_{\kappa,\ell}$ is the (κ,ℓ)-th entry of $\underline{\mathbf{R}}$, z_κ is the κ-th element of $\mathbf{z}$ and $\hat{s}_\ell$ is the ℓ-th element of $\hat{\mathbf{s}}'$.

Regarding complexity, the first important aspect to keep in mind is that the initial value of $\wp$ must be chosen carefully. If this value is too small, then it is possible that no candidate vector is inside of the hypersphere. Moreover, if the initial value of $\wp$ is too large, then the SD complexity becomes high because many nodes must be visited in the tree. As a consequence, an option is to apply a high initial value for $\wp$, e.g., $\wp = \infty$, and then, the radius can be updated as the SD algorithm advances [12]. However, we have determined a simple expression to calculate the initial hypersphere radius, $\wp_0$. Appendix B shows that

$$\wp_0 \ge \sqrt{F^{-1}(1-\epsilon) + \kappa^2 \left(\sigma_c^2+\sigma_n^2\right) \|\hat{\mathbf{s}}'\|^2}, \tag{45}$$

where ϵ is a very small probability and

$$\begin{aligned} F(w) = 1 - \sum_{\ell=0}^{\Upsilon G\mathcal{D}-1} \frac{1}{\ell!} \left[\frac{w}{2(\sigma_c^2+\sigma_n^2)} \right]^\ell \\ \times \exp\left[-\frac{w}{2(\sigma_c^2+\sigma_n^2)} \right], \quad w \ge 0. \end{aligned} \tag{46}$$

Consequently, $F^{-1}(1-\epsilon)$ implies to find the value of w given that $F(w) = 1-\epsilon$. The result of (45) calculates an initial finite hypersphere radius. However, two conditions must be satisfied in order to avoid implementation problems:

1) The probability ϵ must be a very small value. If this condition is not satisfied, then it is highly probable that no candidate vector is inside the hypersphere.
2) The symbol vector $\hat{\mathbf{s}}'$, in (45), must be the candidate vector with highest norm.

In the event in which ϵ is not adequately selected, it is possible that no final node is reached. If this happens, an option is to allocate a value of infinity to $\wp_0$ and then, SD algorithm is executed again. Nevertheless, it represents an increase in the SD algorithm complexity.

V. MEAN BIT ERROR RATE

In this section, an exact closed-form expression to evaluate the PEPs between two multidimensional symbols is derived. Then, an upper bound to calculate the mean BER is obtained. The analysis is made for scenarios where only $\mathcal{U} = 1$ user transmits on a group of G subcarriers in each cell. Thus, there is no presence of MAI but there is presence of CCI. Under some circumstances, the derived expression is an appropriate lower bound for the mean BER of scenarios with presence of MAI, i.e., scenarios where $\mathcal{U} > 1$.

The PEP is the probability of MLD to decide by the erroneous multidimensional symbol $\hat{\mathbf{s}}_i$ given that the multidimensional symbol $\hat{\mathbf{s}}_j$ has been transmitted. As the information of the transmitted multidimensional symbol is available at the receiver only in the received vector $\mathbf{y}$, from (39), the PEP can be written as

$$\mathrm{P}(\hat{\mathbf{s}}_i, \hat{\mathbf{s}}_j) = \mathrm{P}[\, \Phi(\hat{\mathbf{s}}_i) - \Phi(\hat{\mathbf{s}}_j) < 0 | y_1, y_2, \ldots y_{\Upsilon G\mathcal{D}} \,], \tag{47}$$

where y_k is the k-th entry of the received vector $\mathbf{y}$ and

$$\Phi(\hat{\mathbf{s}}) = -\mathbf{y}^T \mathbf{H}' \hat{\mathbf{s}} - (\mathbf{H}'\hat{\mathbf{s}})^T \mathbf{y} + \kappa \left\| \mathbf{H}' \hat{\mathbf{s}} \right\|^2. \tag{48}$$

By calculating the PEPs for different vectors $\hat{\mathbf{s}}_i$ and $\hat{\mathbf{s}}_j$, it is possible to realize that (47) can be rewritten as

$$\mathrm{P}(\hat{\mathbf{s}}_i, \hat{\mathbf{s}}_j) = \mathrm{P}\left[\kappa \sum_{\eta=1}^{\mathcal{D}} \delta_{i,j,\eta}^2 \sum_{a=1}^{\Upsilon} \sum_{g=1}^{G} \alpha_{a,g,\eta}^2 + \sum_{\eta=1}^{\mathcal{D}} \delta_{i,j,\eta} \sum_{a=1}^{\Upsilon} \sum_{g=1}^{G} \alpha_{a,g,\eta} (\mathcal{C}_{a,g,\eta} + n_{a,g,\eta}) < 0 \right], \tag{49}$$

where $\alpha_{a,g,\eta}^2$ is a chi-square random variable with two degrees of freedom $\forall\ a$, g and η. Moreover, $\mathcal{C}_{a,g,\eta}$ and $n_{a,g,\eta}$ denote the CCI and AWGN real samples received in the a-th antenna, g-th subcarrier and η-th dimension, respectively. Additionally, $\delta_{i,j,\eta}$ is the η-th element of the $\mathcal{D}$-dimensional column vector

$$\Delta_{i,j} = \frac{1}{2} \mathbf{W}^T (\hat{\mathbf{s}}_j - \hat{\mathbf{s}}_i). \tag{50}$$

In (49), the terms of the form $\sum_{a=1}^{\Upsilon} \sum_{g=1}^{G} \alpha_{a,g,\eta}^2$ are chi-square random variables with $2\Upsilon G$ degrees of freedom. Hence, the sum of terms into the probability operator at the right-hand side of (49) is similar to the decision variable of a diversity combining system, where the $+1$ symbol was transmitted. Then, the right-hand side of (49) is the probability of that decision variable to be less than 0. Consequently, the PEP can be obtained as the symbol error rate (SER) of a binary antipodal modulation with diversity. In this case, the branches are chi-square random variables with different variances. The factors $\delta_{i,j,\eta}^2$ modify these variances.

The instantaneous SNIR conditioned on the fading amplitudes of the decision variable of (49) is given by

$$\begin{aligned} \gamma_{i,j} &= \frac{\kappa^2 \left(\sum_{\eta=1}^{\mathcal{D}} \delta_{i,j,\eta}^2 \sum_{a=1}^{\Upsilon} \sum_{g=1}^{G} \alpha_{a,g,\eta}^2 \right)^2}{2\mathrm{E}\left\{ \left[\sum_{\eta=1}^{\mathcal{D}} \delta_{i,j,\eta} \sum_{a=1}^{\Upsilon} \sum_{g=1}^{G} \alpha_{a,g,\eta} (\mathcal{C}_{a,g,\eta} + n_{a,g,\eta}) \right]^2 \middle| \alpha_{a,g,\eta} \right\}} \\ &= \frac{\kappa^2}{2(\sigma_n^2 + \sigma_c^2)} \sum_{\eta=1}^{\mathcal{D}} \delta_{i,j,\eta}^2 \sum_{a=1}^{\Upsilon} \sum_{g=1}^{G} \alpha_{a,g,\eta}^2, \end{aligned} \tag{51}$$

where we have used the fact that $\mathcal{C}_{a,g,\eta}$ and $n_{a,g,\eta}$ are independent random variables $\forall a, g, \eta$, that $\mathrm{E}[\mathcal{C}_{a,g,\eta}] = 0$ and that $\mathrm{E}[n_{a,g,\eta}] = 0$, $\forall a, g, \eta$. We have also employed that $\mathrm{E}[n_{a,g,\eta}^2] = \sigma_n^2$ and that $\mathrm{E}[\mathcal{C}_{a,g,\eta}^2] = \sigma_c^2$, $\forall a, g, \eta$, where σ_n^2 and σ_c^2 are given by (14) and (33), respectively.

In (51), each $\alpha_{a,g,\eta}^2$ is given by the sum of two squared real Gaussian random variables, where each random variable has zero-mean and variance σ^2. Thus, we can write that $\alpha_{a,g,\eta}^2 = 2\sigma^2 \tilde{\alpha}_{a,g,\eta}^2 = \sigma_{\mathrm{ch}}^2 \tilde{\alpha}_{a,g,\eta}^2$, where $\sigma_{\mathrm{ch}}^2 = 2\sigma^2$ is the variance of the complex channel gain and $\tilde{\alpha}_{a,g,\eta}^2$ is given by the sum of two zero-mean squared real Gaussian random variables with unit variance. Moreover, in Subsection II-B, it is stated that the symbols belong to a constellation with normalized mean power ($\overline{s^2} = 1$). By the above, (51) can be rewritten as

$$\gamma_{i,j} = \overline{\gamma_c} \sum_{\eta=1}^{\mathcal{D}} \delta_{i,j,\eta}^2 \sum_{a=1}^{\Upsilon} \sum_{g=1}^{G} \tilde{\alpha}_{a,g,\eta}^2, \tag{52}$$

where $\overline{\gamma_c}$ is the mean SNIR per channel, that is given by

$$\begin{aligned} \overline{\gamma_c} &= \frac{\kappa^2 \overline{s^2}}{2(\sigma_n^2 + \sigma_c^2)} \sigma_{\mathrm{ch}}^2 \\ &= \left(\frac{2}{3} \lambda_{\mathcal{I}} \Lambda + \frac{N_0}{E_b} \frac{G}{\log_2 M} \frac{1}{\sigma_{\mathrm{ch}}^2} \right)^{-1}, \end{aligned} \tag{53}$$

where we used (14) and (33). The received symbol energy is $E_s = A^2 \overline{s^2} T_s/2$ and the received energy per bit is $E_b = E_s/\log_2 M$, where M is the modulation order.

In (50), there might be scenarios in which two or more elements of $\Delta_{i,j}$ are equal. As consequence, in (52), there are groups of chi-square random variables with the same variance. Hence, $\gamma_{i,j}$ can be modeled by a generalized chi-square distribution [45], as it is generated by the sum of independent chi-square random variables with different variances and/or different degrees of freedom.

Let $\mathbf{v}_{i,j}$ be a vector containing the elements of $\Delta_{i,j}$ only once. If $\Delta_{i,j}$ has two or more equal elements, they appear only once in $\mathbf{v}_{i,j}$. Further, let $\mathbf{u}$ be a vector where its κ-th element, μ_κ, is the number of times that the κ-th element of $\mathbf{v}_{i,j}$ appears in $\Delta_{i,j}$. Thus, the sum of elements of $\mathbf{u}$ is equal to $\mathcal{D}$. Moreover, in (52), there are ΥG chi-square random variables of the kind $\tilde{\alpha}_{a,g,\eta}^2$ multiplied by different factors $\delta_{i,j,\eta}^2$. Now, we can perform some changes of variables and manipulations on the PDF given by [46, Eq. (6)]. Thus, the PDF of $\gamma_{i,j}$ can be written as

$$\begin{aligned} f(\gamma_{i,j}) = \Omega_{i,j} \sum_{\kappa=1}^{v} \sum_{\ell=1}^{\Upsilon G \mu_k} \frac{\Psi(\kappa, \ell)}{(\Upsilon \mu_\kappa - \ell)!} (-1)^{\Upsilon G \mu_\kappa - 1} \\ \times \frac{(-\gamma_{i,j})^{\Upsilon G \mu_\kappa - \ell}}{\overline{\gamma_c}^{\Upsilon G \mu_\kappa - \ell + 1}} \exp\left(-\frac{\gamma_{i,j}}{\nu_{i,j,\kappa}^2 \overline{\gamma_c}} \right), \quad \gamma_{i,j} \geq 0, \end{aligned} \tag{54}$$

where v and $\nu_{i,j,\kappa}$ are the number of elements of $\mathbf{v}_{i,j}$ and the κ-th element of $\mathbf{v}_{i,j}$, respectively. Additionally, we have that

$$\Omega_{i,j} = \prod_{\kappa=1}^{v} \left(\nu_{i,j,\kappa}^2 \right)^{-\Upsilon G \mu_\kappa} \tag{55}$$

and that

$$\begin{aligned} \Psi(\kappa, \ell) = \sum_{\forall \mathbf{p} \in \zeta_{\kappa,\ell}} \prod_{\substack{m=1 \\ m \neq \kappa}}^{v} \binom{p_m + \Upsilon G \mu_\kappa - 1}{p_m} \\ \times \left(\frac{1}{\nu_{i,j,m}^2} - \frac{1}{\nu_{i,j,\kappa}^2} \right)^{-(\Upsilon G \mu_m + p_m)}, \end{aligned} \tag{56}$$

with $\zeta_{\kappa,\ell} = \left\{ \mathbf{p} \in \mathbb{Z}^v ; \sum_{n=1}^{v} p_n = \ell - 1, p_\kappa = 0, p_n \geq 0, \forall n \right\}$, where p_n is the n-th element of $\mathbf{p}$. Hence, $\zeta_{\kappa,\ell}$ is the set of

$$\mathrm{P}(\hat{\mathbf{s}}_i, \hat{\mathbf{s}}_j) = \Omega_{i,j} \sum_{\kappa=1}^{v} \sum_{\ell=1}^{\Upsilon G \mu_\kappa} \Psi(\kappa, \ell)(-1)^{2\Upsilon G \mu_k - \ell - 1} \left(\nu_{i,j,\kappa}^2\right)^{\Upsilon G \mu_\kappa - \ell + 1} \left(\frac{1-\omega}{2}\right)^{\Upsilon G \mu_\kappa - \ell + 1} \sum_{\tau=0}^{\Upsilon G \mu_\kappa - \ell} \binom{\Upsilon G \mu_\kappa - \ell + \tau}{\tau} \left(\frac{1+\omega}{2}\right)^{\tau} \tag{59}$$

all partitions[6] of length v of the integer $\ell - 1$ [47]. In these partitions, the κ-th element is equal to zero.

As the PEP is obtained as the SER of a binary antipodal modulation with diversity, the PEP conditioned on the instantaneous $\gamma_{i,j}$ can be written as [48, Eq. (5-2-5)]

$$\mathrm{P}(\hat{\mathbf{s}}_i, \hat{\mathbf{s}}_j | \gamma_{i,j}) = \frac{1}{2} \mathrm{erfc}\left(\sqrt{\gamma_{i,j}}\right), \tag{57}$$

where $\mathrm{erfc}(\cdot)$ is the complementary error function [44].

From (54)-(57), the mean PEP can be obtained as

$$\mathrm{P}(\hat{\mathbf{s}}_i, \hat{\mathbf{s}}_j) = \int_0^\infty \mathrm{P}(\hat{\mathbf{s}}_i, \hat{\mathbf{s}}_j | \gamma_{i,j}) f(\gamma_{i,j}) d\gamma_{i,j}, \tag{58}$$

that has closed form and it is given by (59), which is located at the top on this page, where

$$\omega = \left[1 + \left(\overline{\gamma_c}\, \nu_{i,j,\kappa}^2\right)^{-1}\right]^{-\frac{1}{2}}. \tag{60}$$

The mean BER upper bound is obtained as the sum of all PEPs between the set of vectors $\{\hat{\mathbf{s}}_i\}$ that differ at least in their k-th position[7] from $\hat{\mathbf{s}}_j$, for all $\hat{\mathbf{s}}_j$. Therefore, the mean BER upper bound is equal to

$$\overline{P_b} \leq \frac{1}{\sqrt{M}^{\mathcal{D}} \log_2 \sqrt{M}} \sum_i \sum_j \mathrm{P}(\hat{\mathbf{s}}_i, \hat{\mathbf{s}}_j), \tag{61}$$

where $1/\sqrt{M}^{\mathcal{D}}$ is the probability of occurrence of each PEP assuming that all symbols are equally likely and $1/\log_2 \sqrt{M}$ appears because Gray encoding is used in each dimension.

The derivation of the BER expression for $\mathcal{U} > 1$ is quite intricate due to the complicated matrix structure of the received signals. However, numerical results of Section VII show that (61) becomes an appropriate BER lower bound for the scenario $\mathcal{U} > 1$ when the diversity order is high.

VI. ASYMPTOTIC ANALYSIS OF THE BIT ERROR RATE

In this subsection, the asymptote of (61) is derived in order to determine the system diversity. Employing Maclaurin series expansion [40, Eq. (0.318.2)], (60) can be written as

$$\omega = 1 + \sum_{\kappa=1}^{\infty} \mathcal{H}\left(-\frac{1}{2}, \kappa\right) \left(\frac{1}{\overline{\gamma_c}\, \nu_{i,j,\kappa}^2}\right)^{\kappa}, \tag{62}$$

where

$$\mathcal{H}(a, b) = \frac{1}{b!} \prod_{\ell=0}^{b-1} (a - \ell). \tag{63}$$

[6]A partition of a positive integer x, also called an integer partition, is a way of writing x as a sum of positive integers.

[7]The k-th position is always in error. As one symbol error must be ensured at least, any position can be chosen. For simplicity, we can choose $k = 1$.

Replacing (62) in (59) and taking the most significant term of the resulting series,[8] the PEP expression is approximated by

$$\mathrm{P}(\hat{\mathbf{s}}_i, \hat{\mathbf{s}}_j) \approx \frac{1}{2} \Omega_{i,j}\, \mathcal{H}\left(-\frac{1}{2}, \Upsilon G \mathcal{D}\right) \left(\frac{1}{\overline{\gamma_c}}\right)^{\Upsilon G \mathcal{D}}. \tag{64}$$

Additionally, it is possible to show that

$$\mathcal{H}\left(-\frac{1}{2}, \Upsilon G \mathcal{D}\right) = \frac{\sqrt{\pi}\,(1/2 - \Upsilon G \mathcal{D})}{(\Upsilon G \mathcal{D})!\,\Gamma(3/2 - \Upsilon G \mathcal{D})}, \tag{65}$$

where $\Gamma(\cdot)$ is the gamma function [40, eq. (8.310.1)]. Finally, by replacing (65) in (64) and substituting the resulting expression in (61), the mean BER asymptote is given by

$$\overline{P_b} \approx \frac{\sqrt{\pi}\,(1/2 - \Upsilon G \mathcal{D})\,\mathcal{K}}{2\sqrt{M}^{\mathcal{D}} \log_2 \sqrt{M}\,(\Upsilon G \mathcal{D})!\,\Gamma(3/2 - \Upsilon G \mathcal{D})} \left(\frac{1}{\overline{\gamma_c}}\right)^{\Upsilon G \mathcal{D}}, \tag{66}$$

with

$$\mathcal{K} = \sum_i \sum_j \prod_{\kappa=1}^{v} \left(\nu_{i,j,\kappa}^2\right)^{-\Upsilon G \mu_\kappa}, \tag{67}$$

where we also used (55). From (66), the system diversity is $\Upsilon G \mathcal{D}$. If a rotation matrix does not ensures diversity $\mathcal{D}$, $\mathcal{K}$ goes to infinity because some values of $\nu_{i,j,\kappa}$ are zero.

Several rotation matrices present a diversity of order $\mathcal{D}$, but some of them make the system performs better in terms of SNIR. Hence, (67) can be used as a metric to determine the best rotation matrices. Furthermore, unlike the well-known product-distance metric [1], [49], the result of (67) provides direct information about the BER, once it is a factor of its asymptote. Thus, the best rotation matrices can be found by minimizing $\mathcal{K}$. It is interesting to observe that this metric not only depends on the SSD parameters, but also depends on the number of antennas, Υ, and the number of subcarriers, G.

VII. NUMERICAL RESULTS

In this section, the system performance is analyzed with the derived expressions in some relevant scenarios. Monte Carlo simulations verify the expressions accuracy.

A. BEST ROTATION MATRICES

In this subsection, the metric $\mathcal{K}$, defined in (67), is employed to obtain some of the best rotation matrices.

As said in Subsection II-B, the rotation matrices are parameterized by λ variables. In [1], based on the product-distance

[8]This term is the one where the factor $1/\overline{\gamma_c}$ has the least power.

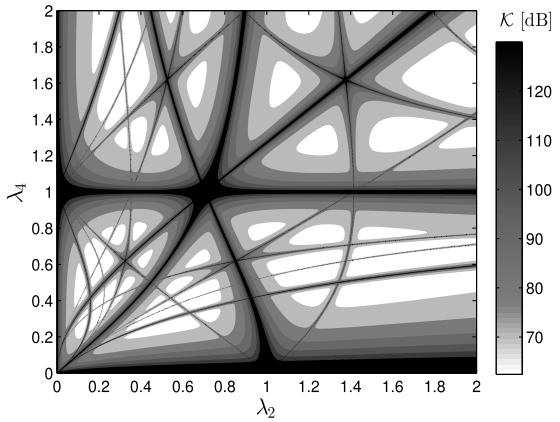

FIGURE 5. Metric $\mathcal{K}$ as a function of λ_2 and λ_4 considering $\Upsilon = 1$, $G = 1$, $\mathcal{D} = 4$ and 4-QAM.

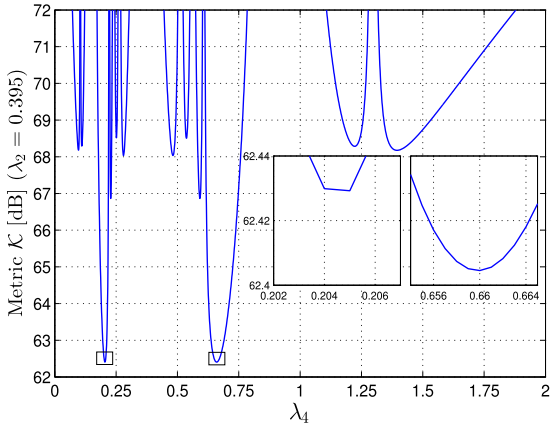

FIGURE 6. Metric $\mathcal{K}$ as a function of λ_4 considering $\lambda_2 = 0.395$, $\Upsilon = 1$, $G = 1$, $\mathcal{D} = 4$ and 4-QAM.

metric, the optimum λs are presented only for 16-QAM and $\mathcal{D} = 2, 3, 4$ and 6. Hence, in this subsection, the optimum λs that generate the best rotation matrices for 4-QAM and 64-QAM are determined for $\mathcal{D} = 2, 3, 4$ and 6 dimensions based on the new metric $\mathcal{K}$. The λs obtained for 16-QAM coincide with those calculated in [1].

Fig. 5 shows $\mathcal{K}$, in dB, as a function of λ_2 and λ_4 for a system with $\Upsilon = 1$, $G = 1$, $\mathcal{D} = 4$ and 4-QAM. The black color denotes regions where the worst rotation matrices appear (highest $\mathcal{K}$). Among these matrices are those that do not generate diversity and hence, they produce $\mathcal{K} = \infty$. Moreover, the white color denote regions where satisfying rotation matrices can be obtained. In these regions, the best rotation matrices can be found. By performing an exhaustive search, we found that the optimum λs for $\mathcal{D} = 4$ and $M = 4$ are $\lambda_2 = 0.395$ and $\lambda_4 = 0.660$. These results are shown in Fig. 6, where $\mathcal{K}$ appears as a function of λ_4 with λ_2 fixed to 0.395, which is its optimum value. In this figure, the regions where the lowest values of $\mathcal{K}$ appear have been amplified.

During the search of the optimum rotation matrices, it was found that different λs appear for different Υ and G. However,

TABLE 1. Optimum λs for different number of dimensions and modulations by considering $\Upsilon = 1$ and $G = 1$.

$\mathcal{D}$	4-QAM	16-QAM [1]	64-QAM
2	$\lambda_2 = 1.932$	$\lambda_2 = 1.618$	$\lambda_2 = 2.634$
3	$\lambda_3 = 1.273$	$\lambda_3 = 0.802$	$\lambda_3 = 0.802$
4	$\lambda_2 = 0.395$, $\lambda_4 = 0.660$	$\lambda_2 = 1.618$, $\lambda_4 = 0.352$	$\lambda_2 = 1.618$, $\lambda_4 = 0.352$
6	$\lambda_3 = 1.526$, $\lambda_6 = 0.180$	$\lambda_3 = 1.526$, $\lambda_6 = 0.180$	$\lambda_3 = 1.526$, $\lambda_6 = 0.180$

TABLE 2. Simulation parameters.

Parameter	Value	Parameter	Value
Number of subcarriers	600	Path-Loss Conditions	SUI Intermediate (Subsection II-C)
Subcarrier bandwidth (B_{sub})	15 kHz	Inner cell radius (R_0)	100 m
Carrier frequency (f_c)	3.5 GHz	Outer cell radius (R)	1000 m
Cyclic prefix duration	5.21 μs	UE antenna height (h_u)	1.5 m
Channel Delay Spread	700 ns	BS antenna height (h_a)	35 m

it was also found that BER values close to the optimum are obtained when the λs calculated for the scenario $\Upsilon = 1$ and $G = 1$ are used. This aspect is shown in more detail in the next subsection. Therefore, since the combinations of Υ and G are infinite, there can be infinite optimal λs depending on these parameters. Thus, in order to guarantee the optimal performance, it is necessary to perform the search using the metric $\mathcal{K}$ defined by (67) with the appropriate system parameters. As an example, Table 1 shows the optimum values of λ for different number of dimensions and modulations by considering $\Upsilon = 1$ and $G = 1$. In order to obtain these results, an exhaustive search has been done considering a resolution of 0.001 for the λ values.

B. SINGLE CELL SCENARIO

The mean BER in single cell scenarios is analyzed in this subsection, i.e., there is presence of MAI, but there is no presence of CCI. Consequently, the use of FFR is not relevant.

The simulation parameters used in this and the following subsection are shown in Table 2. Because the cyclic prefix duration is greater than the channel delay spread, there is no intersymbol interference nor intercarrier interference. Moreover, for simulation purposes, the fading mean power has been normalized to $\sigma_{\text{ch}}^2 = 1$. All simulations are made employing the SD algorithm with an initial radius obtained via (45) with $\epsilon = 10^{-3}$.

Previously, it was indicated that different Υ and G generate different optimal λs. Thus, the aim of Fig. 7 and Fig. 8 is to confirm this assertion. Both figures show the mean BER as a function of E_b/N_0, parameterized by $\mathcal{U}$ and λ_2 considering a system with $\Upsilon = 1, \mathcal{D} = 2$ and 4-QAM. Specifically, the first figure considers $G = 3$ and the second one considers $G = 4$.

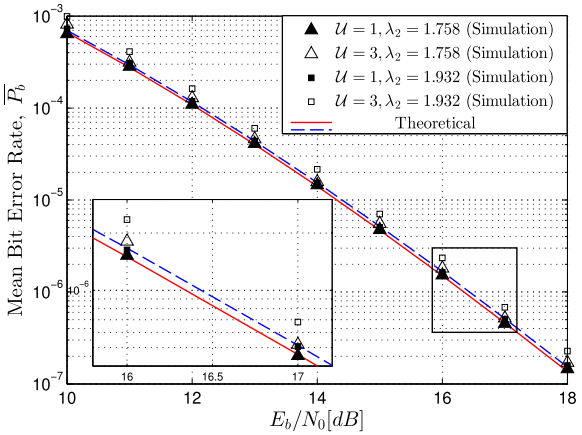

FIGURE 7. Mean BER as a function of E_b/N_0, parameterized by $\mathcal{U}$ and λ_2 considering a system with $\Upsilon = 1$, $G = 3$, $\mathcal{D} = 2$ and 4-QAM.

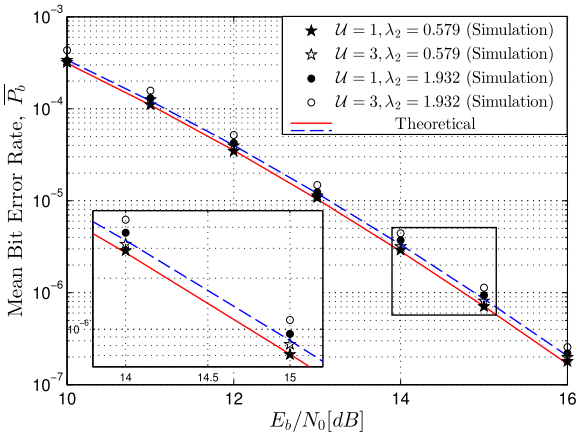

FIGURE 8. Mean BER as a function of E_b/N_0, parameterized by $\mathcal{U}$ and λ_2 considering a system with $\Upsilon = 1$, $G = 4$, $\mathcal{D} = 2$ and 4-QAM.

Theoretical results are shown for $\mathcal{U} = 1$. For the system of Fig. 7, it was determined that the optimum rotation parameter is $\lambda_2 = 1.758$. Thus, note that this scenario has a slightly better performance than the scenario in which the optimal lambda for $\Upsilon = 1$ and $G = 1$ is used (Refer to Table 1). For a better observation of the results, a region has been amplified. For the single user scenario ($\mathcal{U} = 1$), the SNR gain is approximately 0.14 dB. On the other hand, when $\mathcal{U} = 3$, the SNR gain increases to approximately 0.2 dB. For the system of Fig. 8, it was determined that the optimum rotation parameter is $\lambda_2 = 0.579$. Hence, this scenario presents a slightly lower BER than the scenario in which the optimal lambda for $\Upsilon = 1$ and $G = 1$ is employed. Specifically, the SNR gain for $\mathcal{U} = 1$ is approximately 0.12 dB and for $\mathcal{U} = 3$, it is approximately 0.15 dB. Therefore, note that as diversity increases, the SNR gain decreases slightly. The above is an interesting result that cannot be appreciated when using the product distance metric [1] because this metric focuses only on SSD, unlike the metric $\mathcal{K}$ obtained in this work, that considers the number of subcarriers to obtain frequency diversity and the number of reception antennas.

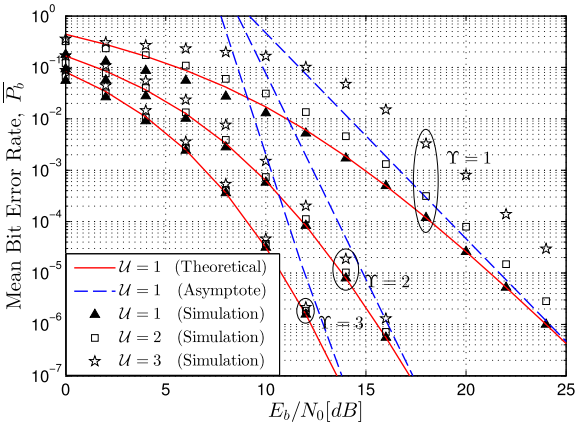

FIGURE 9. Mean BER as a function of E_b/N_0, parameterized by Υ and $\mathcal{U}$ considering a system with $G = 2$, $\mathcal{D} = 2$ and 16-QAM.

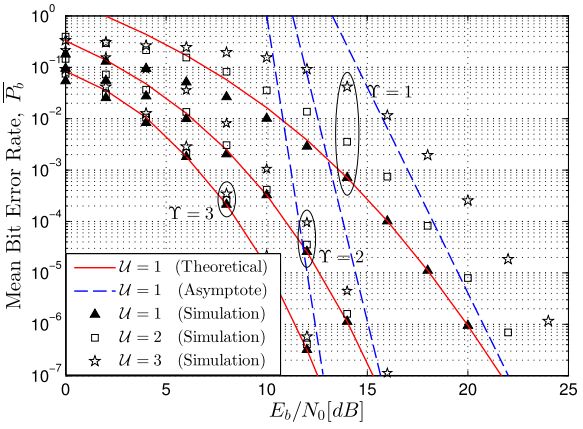

FIGURE 10. Mean BER as a function of E_b/N_0, parameterized by Υ and $\mathcal{U}$ considering a system with $G = 2$, $\mathcal{D} = 4$ and 16-QAM.

In the following, the effects that $\mathcal{U}$ has on the system performance are shown in more detail. As the optimum rotation parameters used for $\Upsilon = 1$ and $G = 1$ allow to obtain near-optimum performance, for simplicity, the λ values shown in Table 1 are used henceforth.

Fig. 9 shows the mean BER as a function of E_b/N_0, parameterized by Υ and $\mathcal{U}$ for an OFDMA system employing 16-QAM, $G = 2$ and $\mathcal{D} = 2$. Fig. 10 shows similar results but considering $\mathcal{D} = 4$. The theoretical BER upper bound and the asymptote for $\mathcal{U} = 1$ are presented along with simulation results for $\mathcal{U} = 1, 2$ and 3 users. Because $G = 2$, there is a scenario in which the system is overloaded, i.e., there are more active users than subcarriers ($\mathcal{U} > G$). It can be achieved because MLD detector is implemented via SD algorithm. For better understanding refer to Subsection IV-B. Specifically, Tikhonov regularization allows the SD algorithm implementation in a multiuser scenario even when $\mathcal{U} > \Upsilon G/2$. Therefore, the system could operate in a multiuser scenario even when $\Upsilon = 1$ and $G = 1$. Consequently, unlike ordinary OFDMA systems that transmit one user information per subcarrier, the proposed system can transmit information from multiple users per subcarrier even without using MIMO ($\Upsilon = 1$). This implies a spectral efficiency increasing.

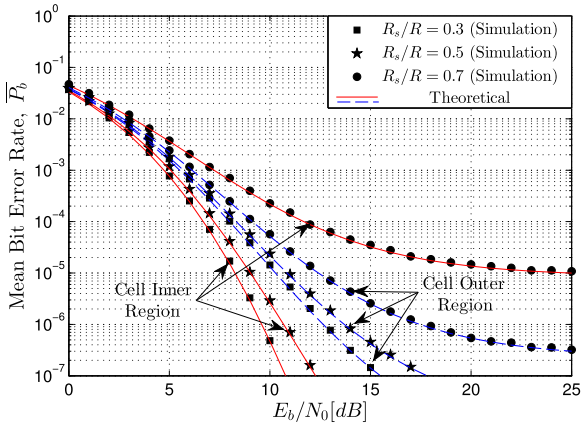

FIGURE 11. Mean BER for CIR and COR as a function of E_b/N_0, parameterized by the ratio R_s/R, considering a system with $\Upsilon = 2$, $G = 4$, $\mathcal{D} = 2$, $\mathcal{U} = 6$ and 4-QAM in FFR cellular scenario.

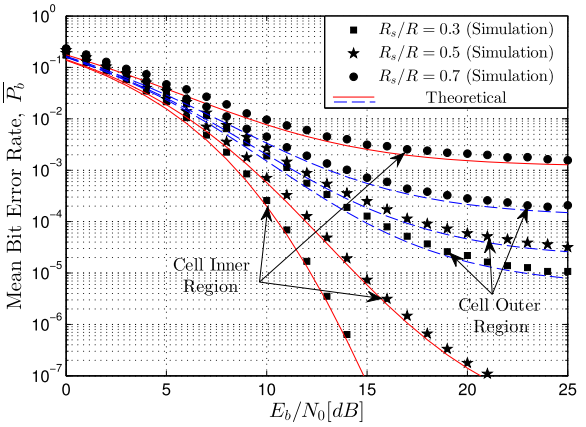

FIGURE 13. Mean BER for CIR and COR as a function of E_b/N_0, parameterized by the ratio R_s/R, considering a system with $\Upsilon = 2$, $G = 4$, $\mathcal{D} = 2$, $\mathcal{U} = 3$ and 16-QAM in FFR cellular scenario.

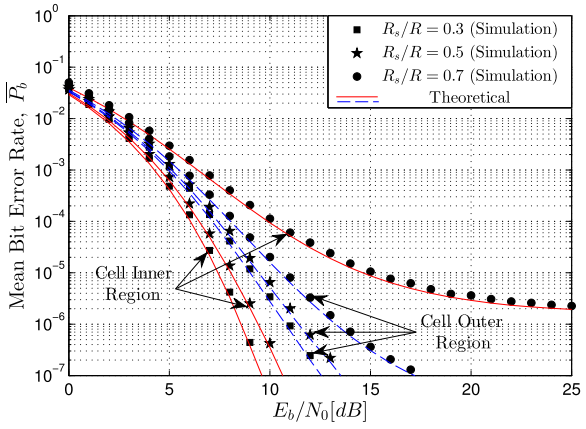

FIGURE 12. Mean BER for CIR and COR as a function of E_b/N_0, parameterized by the ratio R_s/R, considering a system with $\Upsilon = 2$, $G = 8$, $\mathcal{D} = 2$, $\mathcal{U} = 12$ and 4-QAM in FFR cellular scenario.

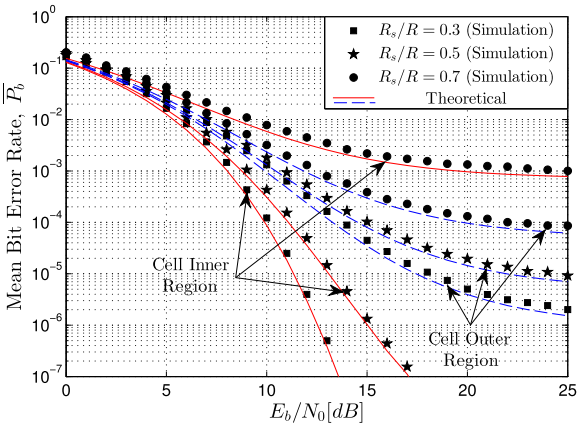

FIGURE 14. Mean BER for CIR and COR as a function of E_b/N_0, parameterized by the ratio R_s/R, considering a system with $\Upsilon = 2$, $G = 8$, $\mathcal{D} = 2$, $\mathcal{U} = 6$ and 16-QAM in FFR cellular scenario.

Observe also that the system does not lose its diversity as $\mathcal{U}$ increases. However, there is a loss in terms of E_b/N_0 when this happens. In addition, as $\mathcal{U}$ increases, the performance degradation becomes smaller as the diversity increases. In this case, notice that the mean BER upper bound for single user becomes an accurate lower bound for scenarios with $\mathcal{U} > 1$.

C. CELLULAR SCENARIO

In this subsection, the BER is evaluated for both regions of the cell of interest for a FFR cellular scenario. It is assumed that the mean number of interferers in each co-cell is equal to the number of active users transmitting over a group of G subcarriers in the cell of interest, i.e., $\lambda_{\mathcal{I}} = \mathcal{U}$.

Fig. 11, 12, 13 and 14 show the mean BER for CIR and COR as a function of E_b/N_0, parameterized by the ratio R_s/R for a system with $\Upsilon = 2$ and $\mathcal{D} = 2$ in a FFR scenario. In particular, Fig. 11 employs $G = 4, \mathcal{U} = 6$ and 4-QAM modulation, Fig. 12: $G = 8, \mathcal{U} = 12$ and 4-QAM, Fig. 13: $G = 4, \mathcal{U} = 3$ and 16-QAM and Fig. 14: $G = 8, \mathcal{U} = 6$ and 16-QAM. Some theoretical curves are plotted, which are the BER upper bound for $\mathcal{U} = 1$, given by (61). As diversity is high in all scenarios, it is interesting to notice that theoretical curves for $\mathcal{U} = 1$ are accurate lower bounds when $\mathcal{U} > 1$. In Fig. 11 and Fig. 13, the diversity is equal to 16. On the other hand, the scenarios presented in Fig. 12 and Fig. 14 have diversity of 32. Note that for a given ratio R_s/R and a given cell region, all scenarios shown in these figures have the same spectral efficiency, which is equal to $\xi = \frac{\mathcal{U}}{G} \log_2 M$ bits/s/Hz. As R_s/R increases, the BER also increases in both cell regions. It occurs because the greater is R_s, the larger is the CIR and as this region employs $\mathcal{F} = 1$, there are high CCI levels. Further, co-cell interferers in the outer regions of the co-cells are quite far from their BS. Hence, they spend high transmission power, producing high CCI. Comparing Fig. 11 with Fig. 12 and Fig. 13 with Fig. 14, notice that even $\mathcal{U}$ is doubled in Fig. 12 and Fig. 14, these scenarios have better performance. This occurs because $G = 8$ is used in these scenarios, which presents higher diversity. From Subsection VII-B, it is known that as diversity increases, the MAI effects become negligible. Moreover, note that increasing diversity also decreases the floors pro-

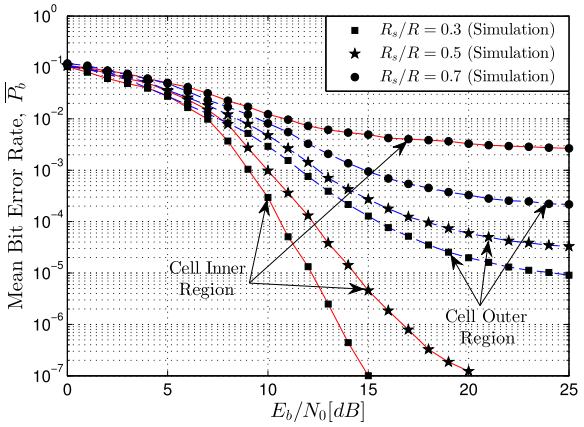

FIGURE 15. Mean BER for CIR and COR as a function of E_b/N_0, parameterized by the ratio R_s/R, considering a system with $\Upsilon = 2$, $G = 8$, $\mathcal{D} = 2$, $\mathcal{U} = 6$ and 16-QAM in FFR cellular scenario. SSD is not employed.

duced by CCI. Consequently, using of frequency diversity and SSD in an OFDMA/MU-MIMO scenario is feasible and improves the cellular system performance. Certainly, a MLD detector using the SD algorithm must be used at the receiver.

Finally, in order to observe the effects of SSD against CCI, Fig. 15 shows the same scenario as Fig. 14, but without employing the SSD technique. In Fig. 15, only results obtained through simulations are presented because the derived BER expression is valid only when SSD is used. Thus, in the figure, the lines are only joining markers for better observation of the results. With respect to the BER expression, if SSD is not employed, then some values of the vector $\mathbf{v}_{i,j}$, used in (56), are equal to zero, which leads to $\Psi(\kappa, \ell) \to \infty$. Consequently, from (59) and (61), we have that $\overline{P_b} \to \infty$. By comparing Fig. 14 (OFDMA with SSD) with Fig. 15 (OFDMA without SSD), note that due to the diversity increasing by SSD, the system can better mitigate the CCI undesirable effects. As result, when OFDMA uses SSD, the floors in the curves appear in lower BER values. As example, for the ratio $R_s/R = 0.3$, $E_b/N_0 = 25$ dB in the cell outer region, the system employing SSD obtains a mean BER of $\overline{P_b} \approx 2 \times 10^{-6}$. On the other hand, the system without SSD obtains $\overline{P_b} \approx 9 \times 10^{-6}$. Moreover, in the first scenario, it is noted that the BER is still decreasing as E_b/N_0 increases. This suggests that the BER floor will be at a lower value. In contrast, the BER floor for the second scenario will be at a value close to $\overline{P_b} \approx 9 \times 10^{-6}$. Performing the above type of comparisons for other modulations, it was observed that as the modulation order decreases, then the improvement in performance increases due to the use of SSD.

VIII. CONCLUSION

Matrix equations that represent the received signals were found for OFDMA/MU-MIMO cellular systems that exploit SSD, spatial and frequency diversities in FFR scenarios. This allowed MLD implementation via SD algorithm. The system model considered the presence of MAI and CCI in a Rayleigh fading scenario. In addition, aspects such as perfect power control and perfect channel estimation are assumed. Although these assumptions can be of a theoretical nature, they are a valid starting point for the mathematical modeling of the proposed multiuser system, since even previous works have analyzed the performance of MIMO and SSD employing only simulations. As result, an exact closed form expression to evaluate the PEPs between two rotated symbols was derived for the scenario $\mathcal{U} = 1$, but considering the presence of CCI. Then, a BER upper bound expression was obtained. The BER asymptotic analysis showed that the system diversity is equal to $\Upsilon G\mathcal{D}$. With this analysis, it was also found that the optimum rotation matrices for the SSD technique can vary depending on the system parameters, that is, Υ, G or $\mathcal{D}$. Moreover, it was observed that the system does not lose diversity as $\mathcal{U}$ increases. As consequence, if the diversity order is much greater than $\mathcal{U}$, the system performance for $\mathcal{U} > 1$ is very similar to the performance for $\mathcal{U} = 1$. Therefore, the BER upper bound expression is an accurate lower bound for scenarios where $\Upsilon G\mathcal{D} \gg \mathcal{U}$. In addition, it was observed that CCI produces floors in the BER curves that cannot be eliminated even increasing the E_b/N_0, once MLD removes only MAI. However, these floors appear in lower BER values when FFR and SSD are used. Finally, the considered cellular system not only improves the system performance in terms of the mean BER, but also improves the spectral efficiency when compared to ordinary OFDMA cellular systems, because in our approach, the system can be overloaded. Therefore, the number of active users transmitting simultaneously may be greater than the number of subcarriers in the system ($\mathcal{U} > G$). This overload can arise even when $\Upsilon = 1$ antenna is used at the receiver. In particular, it is also possible for several users to transmit simultaneously on the same subcarrier even when $G = 1$ and $\Upsilon = 1$.

APPENDIX A
CO-CELL INTERFERENCE VARIANCE

The CCI variance per channel (σ_c^2) is obtained in this appendix. The CCI sample received at the a-th antenna and g-th subcarrier during the η-th time slot is defined in two time intervals (refer to Fig. 4). During $\tau \le t \le \zeta_\ell$, it is given by

$$\mathcal{C}_{a,g,\eta}(t) = \frac{A}{\sqrt{G}} \sum_{\ell=1}^{\mathcal{N}_\mathcal{I}} \sqrt{\rho_\ell^\beta d_\ell^{-\beta}}\, \mathcal{G}_{a,g,\eta,\ell} \times \Re\{\tilde{r}_{\eta,\ell} \exp\left[\mathbf{i}\, 2\pi \left(f_c + g\Delta_{f_i}\right) t\right] p(t - \zeta_\ell + T_s)\}, \tag{68a}$$

and during the interval $\zeta_\ell < t \le \tau + T_s$, it is written as

$$\mathcal{C}'_{a,g,\eta}(t) = \frac{A}{\sqrt{G}} \sum_{\ell=1}^{\mathcal{N}_\mathcal{I}} \sqrt{\rho_\ell^\beta d_\ell^{-\beta}}\, \mathcal{G}'_{a,g,\eta,\ell} \times \Re\{\tilde{r}'_{\eta,\ell} \exp\left[\,\mathbf{i}\, 2\pi \left(f_c + g\Delta_{f_i}\right) t\,\right] p(t - \zeta_\ell)\}, \tag{68b}$$

After the demodulation stage, the received sample is given by

$$\mathcal{C}_{a,g,\eta} = \frac{1}{T_s}\int_{\tau}^{\tau+T_s}\left[\mathcal{C}_{a,g,\eta}(t)+\mathcal{C}'_{a,g,\eta}(t)\right] \times \exp\left[-\mathbf{i}\,2\pi\left(f_c+g\Delta_{fi}\right)t\right]p(t-\tau)dt. \quad (69)$$

The in-phase component of the above sample is

$$\mathcal{C}_{a,g,,\eta,\mathrm{P}} = \frac{A}{2\sqrt{G}}\sum_{\ell=1}^{\mathcal{N}_{\mathcal{I}}}\alpha_{a,g,\eta,\ell}P(\ell) \times\left[\tilde{r}_{\eta,\ell,\mathrm{P}}\cos(\phi_{a,g,\eta,\ell})-\tilde{r}_{\eta,\ell,\mathrm{Q}}\sin(\phi_{a,g,\eta,\ell})\right] + \frac{A}{2\sqrt{G}}\sum_{\ell=1}^{\mathcal{N}_{\mathcal{I}}}\alpha'_{a,g,\ell}P'(\ell) \times\left[\tilde{r}'_{\eta,\ell,\mathrm{P}}\cos(\phi'_{a,g,\eta,\ell})-\tilde{r}'_{\eta,\ell,\mathrm{Q}}\sin(\phi'_{a,g,\eta,\ell})\right], \quad (70)$$

where $P(\ell)$ and $P'(\ell)$ are given by (20) and (21), respectively. We have employed (7) and that $\tilde{r}_{\eta,\ell} = \tilde{r}_{\eta,\ell,\mathrm{P}} + \mathbf{i}\,\tilde{r}_{\eta,\ell,\mathrm{Q}}$, i.e., $\tilde{r}_{\eta,\ell,\mathrm{P}}$ and $\tilde{r}_{\eta,\ell,\mathrm{Q}}$ are the in-phase and quadrature components of $\tilde{r}_{\eta,\ell}$. For better understanding refer to (32).

From (70), the mean value of the CCI is zero because $\overline{\cos(x)} = \overline{\sin(x)} = 0$ when x is a uniformly distributed random variable over $[0, 2\pi)$. Moreover, the variance of the CCI sample is equal to

$$\sigma_c^2 = \frac{A^2}{8G}\lambda_{\mathcal{I}}\,\sigma_{\mathrm{ch}}^2\,\overline{\tilde{r}_{\eta,\ell}^2}\,\mathrm{E}\left[\left(\frac{\zeta_\ell-\tau}{T_s}\right)+\left(\frac{\tau+T_s-\zeta_\ell}{T_s}\right)\right]\Lambda, \quad (71)$$

with

$$\Lambda = \sum_{j=1}^{6}\mathrm{E}\left[\rho^{\beta}d^{-\beta}\left(R_{\mathrm{i}},R_{\mathrm{f}},\mathcal{F}\right)\right]_j. \quad (72)$$

where we used (11) with $\overline{\mathcal{I}_j} = \lambda_{\mathcal{I}}$. We have also used (20) and (21), that $\overline{\cos(x)\sin(y)} = 0$, and that $\overline{\cos^2(x)} = \overline{\sin^2(x)} = 1/2$ when x and y are independent uniformly distributed random variables over $[0, 2\pi)$. It was used that $\overline{\alpha_{a,g,\eta,\ell}^2} = \overline{\alpha_{a,g,\eta,\ell}'^2} = \sigma_{\mathrm{ch}}^2$ and that $\overline{\tilde{r}_{\eta,\ell}^2} = \overline{\tilde{r}_{\eta,\ell,\mathrm{P}}^2} + \overline{\tilde{r}_{\eta,\ell,\mathrm{Q}}^2}$. Furthermore, the factor $\rho^{\beta}d^{-\beta}$ is a function of R_{i}, R_{f} and $\mathcal{F}$. In the mean of $\rho^{\beta}d^{-\beta}$, in (72), the subscript j indicates that the mean value is related to the j-th co-cell of the first layer.

The rotation and interleaving processes do not modify the mean power of the transmitted symbols. Then, $\overline{\tilde{r}_{\eta,\ell}^2} = \overline{s^2}$. In addition, in (71), ζ_ℓ is a random variable uniformly distributed over $[\tau, \tau + T_s]$. As consequence, (71) can be rewritten as (33).

From (2)-(4), $\mathrm{E}\left[\rho^{\beta}d^{-\beta}\left(R_{\mathrm{i}},R_{\mathrm{f}},\mathcal{F}\right)\right]_j$ in (72) is obtained as

$$\mathrm{E}\left[\rho^{\beta}d^{-\beta}\left(R_{\mathrm{i}},R_{\mathrm{f}},\mathcal{F}\right)\right]_j = \int_{R_{\mathrm{i}}}^{R_{\mathrm{f}}}\int_0^{2\pi}F(\rho,\theta,j,\mathcal{F},\beta) \times f(\rho;R_{\mathrm{i}},R_{\mathrm{f}})f(\theta)d\rho d\theta, \quad (73)$$

where

$$F(\rho,\theta,j,\mathcal{F},\beta) = \left\{\frac{r^2}{D^2+\rho^2+2D\rho\cos\left[\theta-\Omega-(j-1)\frac{\pi}{3}\right]}\right\}^{\frac{\beta}{2}}. \quad (74)$$

Considering that $x^{-s} = \frac{1}{\Gamma(s)}\int_0^{\infty}y^{s-1}e^{-xy}dy$, for $x > 0$ [40], where $\Gamma(.)$ denotes the gamma function and after some manipulations, it is possible to rewrite (73) as (35).

APPENDIX B
INITIAL HYPERSPHERE RADIUS FOR THE SPHERE DECODER ALGORITHM

In this appendix, we obtain a simple expression to calculate the initial hypersphere radius, $\wp_0$, for the SD algorithm. Due to the extended channel (Tikhonov regularization), we can state that a symbol vector is inside of the hypersphere if $\left\|\underline{\mathbf{y}}-\kappa\underline{\mathbf{H}}\hat{\mathbf{s}}\right\|^2 \leq \wp_0^2$, with $\underline{\mathbf{y}} = (\mathbf{y},\ \mathbf{0}_{2\mathcal{DU}})^T$, where $\mathbf{0}_{2\mathcal{DU}}$ is a $2\mathcal{DU}\times 1$ null vector and $\underline{\mathbf{H}}$ is given by (43). Now, we consider the next condition:

$$\mathrm{P}\left[\wp_0^2 < \left\|\underline{\mathbf{y}}-\kappa\underline{\mathbf{H}}\hat{\mathbf{s}}'\right\|^2\right] \leq \epsilon, \quad (75)$$

where ϵ is a very small probability. From (38) and (43), if the detector decides correctly by the transmitted symbol vector, then we can write

$$\mathrm{P}\left[\wp_0^2 < \left\|\underline{\mathbf{y}}-\kappa\underline{\mathbf{H}}\hat{\mathbf{s}}'\right\|^2\right] = \mathrm{P}\left[\wp_0^2 < \|\mathbf{w}\|^2+\kappa^2\left(\sigma_c^2+\sigma_n^2\right)\|\hat{\mathbf{s}}'\|^2\right] \quad (76)$$

where $\mathbf{w} = \mathbf{C}+\mathbf{n}$, i.e., $\mathbf{w}$ is a $\Upsilon G\mathcal{D}\times 1$ vector containing the samples of the CCI plus noise. As CCI and noise samples are independent zero-mean complex Gaussian random variables, the elements of $\mathbf{w}$ are also zero-mean complex Gaussian random variables with variance $\sigma_c^2+\sigma_n^2$. Therefore, $w = \|\mathbf{w}\|^2$ is a chi-square random variable with $2\Upsilon G\mathcal{D}$ degrees of freedom with cumulative distribution function (CDF) given by (46) [44]. Hence, using (46), we can rewrite (76) as

$$\mathrm{P}\left[\wp_0^2 < \left\|\underline{\mathbf{y}}-\kappa\underline{\mathbf{H}}\hat{\mathbf{s}}'\right\|^2\right] = \mathrm{P}\left[w > \wp_0^2-\kappa^2\left(\sigma_c^2+\sigma_n^2\right)\|\hat{\mathbf{s}}'\|^2\right] = 1-F\left(\wp_0^2-\kappa^2\left(\sigma_c^2+\sigma_n^2\right)\|\hat{\mathbf{s}}'\|^2\right). \quad (77)$$

Consequently, with (77), (75) can be rewritten as

$$1-F\left(\wp_0^2-\kappa^2\left(\sigma_c^2+\sigma_n^2\right)\|\hat{\mathbf{s}}'\|^2\right) \leq \epsilon, \quad (78)$$

Finally, the initial hypersphere radius is calculated by (45).

REFERENCES

[1] J. Boutros and E. Viterbo, "Signal space diversity: A power- and bandwidth-efficient diversity technique for the Rayleigh fading channel," *IEEE Trans. Inf. Theory*, vol. 44, no. 4, pp. 1453–1467, Jul. 1998.

[2] Z. Liu, Y. Xin, and G. B. Giannakis, "Linear constellation precoding for OFDM with maximum multipath diversity and coding gains," *IEEE Trans. Commun.*, vol. 51, no. 3, pp. 416–427, Mar. 2003.

[3] T. V. K. Chaitanya, D. Danev, and E. G. Larsson, "Constant envelope signal space diversity," in *Proc. IEEE ICASSP*, May 2014, pp. 3147–3151.

[4] K. N. Pappi, N. D. Chatzidiamantis, and G. K. Karagiannidis, "Error performance of multidimensional lattice constellations—Part I: A parallelotope geometry based approach for the AWGN channel," *IEEE Trans. Commun.*, vol. 61, no. 3, pp. 1088–1098, Mar. 2013.

[5] K. N. Pappi, N. D. Chatzidiamantis, and G. K. Karagiannidis, "Error performance of multidimensional lattice constellations—Part II: Evaluation over fading channels," *IEEE Trans. Commun.*, vol. 61, no. 3, pp. 1099–1110, Mar. 2013.

[6] M. A. Khan, "Secrecy enhancement of dual-hop cooperative relay system using signal space diversity," in *Proc. 16th IEEE Annu. Consum. Commun. Netw. Conf. (CCNC)*, Jan. 2019, pp. 1–4.

[7] M. A. Khan, H. LeBlanc, and F. Hassan, "Signal space diversity based cognitive two-way relay network with underlay spectrum sharing," in *Proc. 16th IEEE Annu. Consum. Commun. Netw. Conf. (CCNC)*, Jan. 2019, pp. 1–6.

[8] S. Özyurt and O. Kucur, "Performance of OFDM with signal space diversity using subcarrier coordinate interleaving," *IEEE Trans. Veh. Technol.*, vol. 67, no. 10, pp. 10134–10138, Oct. 2018.

[9] Z. Ye, T. Arbi, F.-X. Socheleau, and B. Geller, "Fast soft demapping for underwater acoustic communications with signal space diversity," in *Proc. MTS/IEEE Charleston OCEANS*, Oct. 2018, pp. 1–6.

[10] S. Verdu, *Multiuser Detection*. Cambridge, U.K.: Cambridge Univ. Press, 1998.

[11] H. Carvajal M., N. Orozco G., and C. de Almeida, "Signal space diversity in single and multiuser scenarios employing sphere decoder detector," *IEEE Commun. Lett.*, vol. 22, no. 4, pp. 868–871, Apr. 2018.

[12] E. Viterbo and J. Boutros, "A universal lattice code decoder for fading channels," *IEEE Trans. Inf. Theory*, vol. 45, no. 5, pp. 1639–1642, Jul. 1999.

[13] H. Nikopour and H. Baligh, "Sparse code multiple access," in *Proc. IEEE 24th PIMRC*, Sep. 2013, pp. 332–336.

[14] A. Gupta and E. R. K. Jha, "A survey of 5G network: Architecture and emerging technologies," *IEEE Access*, vol. 3, pp. 1206–1232, 2015.

[15] H. Wu, X. Xiong, and H. Gao, "Low complexity detection based on selective message passing for SCMA systems," *Electron. Lett.*, vol. 54, no. 8, pp. 533–535, 2018.

[16] S. Sharmila and C. V. Lakshmi, "Performance analysis of QoS based frequency diversity selectivity scheduling in LTE downlink systems," in *Proc. ICECS*, 2014, pp. 1–5.

[17] Y.-W. Kuo, C. C. Lu, and G.-Y. Shen, "Adaptive resource allocation for downlink grouped MC-CDMA systems with power and BER constraints," *Int. J. Electron. Commun.*, vol. 68, no. 1, pp. 25–32, 2014.

[18] C. Gueguen, M. Ezzaouia, and M. Yassin, "Inter-cellular scheduler for 5G wireless networks," *Phys. Commun.*, vol. 18, no. 2, pp. 113–124, 2016.

[19] R. Ghaffar and R. Knopp, "Fractional frequency reuse and interference suppression for OFDMA networks," in *Proc. 8th WiOpt*, 2010, pp. 273–277.

[20] H. Holma, A. Toskala, and J. Reunanen, *LTE Small Cell Optimization: 3GPP Evolution to Release 13*. West Sussex, U.K.: Wiley, 2016.

[21] T. Rappaport, *Wireless Communications: Principles and Practice*. Upper Saddle River, NJ, USA: Prentice-Hall, 1996.

[22] M. D. Yacoub, *Wireless Technology: Protocols, Standards, and Techniques*. Boca Raton, FL, USA: CRC Press, 2012.

[23] M. M. da Silva and F. A. Monteiro, *MIMO Processing for 4G and Beyond: Fundamentals and Evolution*. Boca Raton, FL, USA: CRC Press, 2014.

[24] J.-Y. Choi, J.-S. Baek, and J.-S. Seo, "A new layered MIMO-OFDM system with signal space diversity," *IEICE Electron. Express*, vol. 8, no. 1, pp. 26–32, 2011.

[25] Z. Wu and X. Gao, "An efficient MIMO scheme with signal space diversity for future mobile communications," *EURASIP J. Wireless Commun. Netw.*, vol. 2015, p. 87, Dec. 2015.

[26] G. Krishna, K. V. Srinivas, S. Bhashyam, and R. D. Koilpillai, "Signal space diversity for spatial multiplexing," in *Proc. IEEE 19th PIMRC*, Sep. 2018, pp. 1–5.

[27] L. Zheng and D. N. C. Tse, "Diversity and multiplexing: A fundamental tradeoff in multiple-antenna channels," *IEEE Trans. Inf. Theory*, vol. 49, no. 5, pp. 1073–1096, May 2003.

[28] S. Özyurt and O. Kucur, "Performance analysis of signal space diversity with transmit antenna selection and maximal ratio combining," in *Proc. 25th Signal Process. Commun. Appl. Conf. (SIU)*, 2017, pp. 1–4.

[29] S. Özyurt and O. Kucur, "Performance analysis of maximal ratio combining with transmit antenna selection and signal space diversity under exponential antenna correlation," *IET Commun.*, vol. 12, no. 5, pp. 612–619, 2018.

[30] S. Özyurt, "Performance analysis of zero-forcing precoding with signal space diversity under antenna correlation," *Phys. Commun.*, vol. 30, pp. 115–121, Oct. 2018.

[31] T. D. Novlan, R. K. Ganti, A. Ghosh, and J. G. Andrews, "Analytical evaluation of fractional frequency reuse for heterogeneous cellular networks," *IEEE Trans. Commun.*, vol. 60, no. 7, pp. 2029–2039, Jul. 2012.

[32] N. Yee, J. M. G. Linnartz, and G. P. Fettweis, "Multi-carrier CDMA in indoor wireless radio networks," in *Proc. IEEE Pers. Indoor Mobile Radio Commun. (PIMRC)*, Yokohama, Japan, Sep. 1993, pp. 109–113.

[33] *LTE—Evolved Universal Terrestrial Radio Access (E-UTRA) and Evolved Universal Terrestrial Radio Access Network (E-UTRAN): Overall Description*, document 3GPP TS 36.300 Version 13.2.0 Release, 3GPP, 2016, vol. 13.

[34] H. Holma and A. Toskala, *LTE for UMTS: Evolution to LTE–Advanced*. Hoboken, NJ, USA: Wiley, 2011.

[35] *LTE—Evolved Universal Terrestrial Radio Access (E-UTRA): Physical Layer Procedures*, document 3GPP TS 36.213 Version 13.2.0 Release, 3GPP, 2016, vol. 13.

[36] J. S. Seybold, *Introduction to RF Propagation*. Hoboken, NJ, USA: Wiley, 2005.

[37] P. D. Katev, "Propagation models for WiMAX at 3.5 GHz," in *Proc. IEEE Elektro Conf.*, May 2012, pp. 61–65.

[38] *5G Spectrum GSMA Public Policy Position*, GSM Assoc., London, U.K., Nov. 2016.

[39] M. G. Jansen and R. Prasad, "Capacity, throughput, and delay analysis of a cellular DS CDMA system with imperfect power control and imperfect sectorization," *IEEE Trans. Veh. Technol.*, vol. 44, no. 1, pp. 67–75, Feb. 1995.

[40] I. Gradshteyn and I. Ryzhik, *Table of Integrals, Series, and Products*, 7th ed. London, U.K.: Elsevier, 2007.

[41] G. H. Golub, P. C. Hansen, and D. P. O'Leary, "Tikhonov regularization and total least squares," *SIAM J. Matrix Anal. Appl.*, vol. 21, no. 1, pp. 185–194, 1999.

[42] D. Wubben, R. Bohnke, V. Kuhn, and K.-D. Kammeyer, "MMSE extension of V-BLAST based on sorted QR decomposition," in *Proc. IEEE 58th VTC-Fall*, Oct. 2003, pp. 508–512.

[43] E. Zimmermann, *Complexity Aspects in Near Capacity MIMO Detection Decoding*. Dresden, Germany: Dresden Univ. Technology, 2007.

[44] A. Papoulis and S. Pillai, *Probability—Random Variables and Stochastic Processes*, 4th ed. New York, NY, USA: McGraw-Hill, 2002.

[45] R. Davies, "Algorithm AS155: The distribution of a linear combination of X^2 random variables," *Appl. Statist.*, vol. 29, no. 3, pp. 323–333, 1980.

[46] E. Björnson, D. Hammarwall, and B. Ottersten, "Exploiting quantized channel norm feedback through conditional statistics in arbitrarily correlated MIMO systems," *IEEE Trans. Signal Process.*, vol. 57, no. 10, pp. 4027–4041, Oct. 2009.

[47] G. Andrews and K. Eriksson, *Integer Partitions*. New York, NY, USA: Cambridge Univ. Press, 2004.

[48] J. Proakis and D. Manolakis, *Digital Signal Processing*, 4th ed. New York, NY, USA: McGraw-Hill, 2007.

[49] E. Bayer-Fluckiger, F. Oggier, and E. Viterbo, "New algebraic constructions of rotated Zn-lattice constellations for the Rayleigh fading channel," *IEEE Trans. Inf. Theory*, vol. 50, no. 4, pp. 702–714, Apr. 2004.

HENRY CARVAJAL MORA received the B.Sc. degree (Hons.) in electronics and telecommunications engineering from Armed Forces University-ESPE, Sangolquí, Ecuador, in 2009, and the M.Sc. and Ph.D. degrees in electrical engineering from the School of Electrical and Computer Engineering (FEEC), University of Campinas (UNICAMP), Brazil, in 2014 and 2018, respectively. In 2018, he was the Director of technology transfer area with the Education, Science, Technology, and Innovation Secretariat (SENESCYT), Ecuador. He is currently a Full Professor with the Universidad de Las Américas (UDLA), Quito, Ecuador. His research interests include diversity-combining systems, multiple access systems, multiuser detection, MIMO systems, and 5G communications systems.

NATHALY OROZCO G. received the Electronic and Telecommunications Engineering degree from Armed Forces University-ESPE, Sangolquí, Ecuador, in 2011, and the M.Sc. and Ph.D. degrees in electrical engineering from the University of Campinas (UNICAMP), Brazil, in 2014 and 2018, respectively. She is currently a Full Professor with the Universidad de Las Américas (UDLA), Quito, Ecuador. Her research interests include digital communications with a specific emphasis on multiple access techniques, fading channels, MIMO, cognitive opportunistic wireless systems, and 5G technologies.

PAULO CHILIGUANO T. received the B.Sc. degree in electrical engineering and telecommunications from Armed Forces University-ESPE, Sangolquí, Ecuador, in 2009, and the M.Sc. degree in sound and music computing from the School of Electronic Engineering and Computer Science (EECS), Queen Mary University of London (QMUL), London, U.K. He was a Telecommunications Engineer in the industry, from 2010 to 2014. His current research interests include digital communications, digital signal processing, audio technology, and machine learning.

CELSO DE ALMEIDA received the Electrical Engineering degree and the M.Sc. and Ph.D. degrees from the State University of Campinas (UNICAMP), Brazil, in 1980, 1983, and 1990, respectively. He was an Electrical Engineer with optical communications, in the industry, from 1982 to 1990. He joined the Electrical Engineering Faculty, UNICAMP, in 1990, where he is currently a Full Professor. His research interests include cellular systems, CDMA, OFDMA, multiuser detection, antenna arrays, MIMO systems, wireless communications, cryptography, and error correction codes.